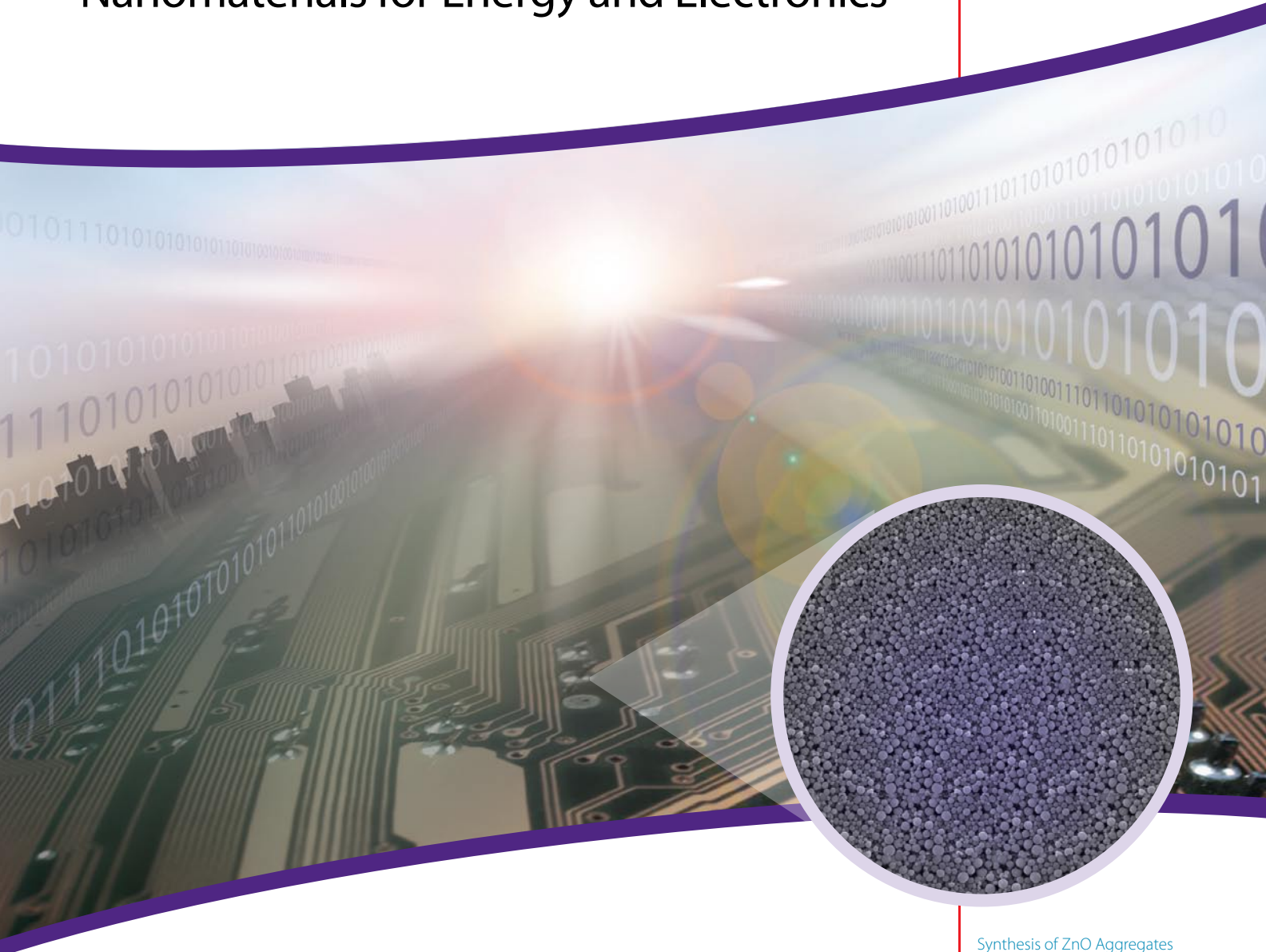


Material Matters™

Volume 5, Number 2 • 2010



Nanomaterials for Energy and Electronics



Shining light on nanomaterials

Synthesis of ZnO Aggregates
and Their Application in
Dye-sensitized Solar Cells

Nanomaterials for Energy
Storage in Lithium-ion Battery
Applications

Synthesis, Properties, and
Applications of Perovskite-phase
Metal Oxide Nanostructures

Introduction

Welcome to the issue of *Material Matters*[™] focusing on Nanomaterials for Energy and Electronics.

The term *nanomaterials* defines an extremely diverse group of materials, where morphological features do not exceed 100 nanometers.¹ The idea of manipulating materials on the atomic level goes back to Richard Feynman and his prominent lecture "There's Plenty of Room at the Bottom".² However, the boom of nanomaterials began only in the 1990s and quickly spread out into a vast majority of modern technologies including energy and electronics. The main reasons for the rapid expansion of nanomaterials into different application areas are the unique properties stemming from nanoscale dimensions. Nanoparticles and nanostructures demonstrate an extremely high surface-to-volume ratio, enabling quantum effects that are impossible in the conventional, micrometer-sized materials. As an example, particles of crystalline BaTiO₃ usually have a cubic structure at their surface, but are tetragonal-ordered in the bulk. As the particle size decreases, the content of the cubic phase gradually increases until the tetragonal phase completely disappears when BaTiO₃ particles enter the nanosize region. The disappearance of the tetragonal phase changes the magnetic properties of the material, which becomes super-paraelectric (vs. ferroelectric in the conventional titanate).³ Another reason for growing interest in nanoscale materials is device miniaturization in the electronics industry. In agreement with the famous Moore's Law,⁴ the number of transistors placed on an integrated circuit doubles every 24 months, which is possible only through the continuous miniaturization of all elements forming the circuit. Use of nanomaterials and nanostructures is one of the most attractive ways to sustain progress in this field.

Other fast growing research areas using nanomaterials include energy storage and conversion. Today, most high-efficiency solar cells and battery systems include nanomaterials as essential components. It has been clearly shown⁵ that the efficiency of a dye-sensitized solar cell can strongly depend on the size of titanium or zinc oxide particles used in the cell's design. Nanomaterials also significantly enhance energy storage capacities and electrochemical performance of lithium-ion batteries. The formation of highly disordered and/or amorphous phases in battery electrode materials is desirable and the use of nanostructured materials offers an excellent way to achieve it.⁶

The current issue of *Material Matters*[™] features three articles that highlight nanomaterials for photovoltaics, Li-ion batteries, and electronics applications. Zinc oxide aggregates and their applications in dye-sensitized solar cells are discussed in a comprehensive review by the group of Prof. Guozhong Cao from the University of Washington. Dr. Ganesh Venugopal and Dr. Andrew Hunt from nGimat and Prof. Faisal Alamgir from Georgia Tech highlight the use of nanomaterials for energy storage in Li-ion batteries. Finally, the synthesis and properties of perovskite-phase metal oxide nanostructures are reviewed in the article by Dr. Yuanbing Mao, Dr. Hongjun Zhou, and Prof. Stanislaus S. Wong from the State University of New York at Stony Brook.

The "Your Materials Matter" section of this issue features a material that has been brought to our attention by a leading researcher from the scientific community. Each article in this publication is accompanied by the relevant Aldrich® Materials Science products. The opposing page lists the material categories that you will find in this issue. For a comprehensive library of products and additional information, please visit Aldrich Materials Science at aldrich.com/matsci. We welcome your comments and questions regarding *Material Matters*[™] or any materials of interest. Please contact us at matsci@sial.com.

References

- (1) The threshold for nanoscale materials is usually set at 100 nm, though the term is sometimes used for the dimensions smaller than one micrometer.
- (2) Feynman, R. in *Miniaturization*, Gilbert, H. D., Ed.; Reinhold Publishing Corporation, New York, 1961.
- (3) Mao, Y.; Zhou, H.; Wong, S.S. Perovskite-phase Metal Oxide Nanostructures: Synthesis, Properties, and Applications, *Material Matters* 2010, 5.2, 50-54.
- (4) Moore, G. E. *Electronics*, 1965, 38, 114.
- (5) Zhang, Q.; Park, K.; Dandeneau, C.S.; Yodyingyong, S.; Liu, D.; Zhou, X.; Jeong, Y.-H.; Cao, G. Synthesis of ZnO Aggregates and Their Application in Dye-sensitized Solar Cells, *Material Matters* 2010, 5.2, 32-40.
- (6) Dillon, A. C.; Ban, C.; Riley, L.A.; Wu, Z.; Gillaspie, D.T.; Chen, L.; Yan, Y.; Le, S. High energy density metal oxide anodes for Li-ion batteries. at *Materials Challenges in Alternative & Renewable Energy*, Cocoa Beach, Florida, February 21-24, 2010.

About Our Cover

Progress in the area of nanomaterials has pervaded the vast majority of technologies, from electronics to energy generation and storage. Over the last decade, the ability to manipulate and control materials at an atomic level has allowed for both the reduction in size and the increase in efficiency of electronic devices, solar cells and batteries, thus, revolutionizing the traditional way of living. Nanopowders (shown on the cover) are key elements to a diverse set of technology areas enabling high-density storage of information (see p. 50), conversion of solar light into electricity (p. 32) and storing it for later use (p. 42).



Viktor Balema
Materials Science
Sigma-Aldrich Corporation

Material Matters[™]

Vol. 5, No. 2 • 2010

Aldrich Chemical Co., Inc.
Sigma-Aldrich Corporation
6000 N. Teutonia Ave.
Milwaukee, WI 53209, USA

To Place Orders

Telephone 800-325-3010 (USA)
FAX 800-325-5052 (USA)

Customer & Technical Services

Customer Inquiries 800-325-3010
Technical Service 800-231-8327
SAFC® 800-244-1173
Custom Synthesis 800-244-1173
Flavors & Fragrances 800-227-4563
International 414-438-3850
24-Hour Emergency 414-438-3850
Website sigma-aldrich.com
Email aldrich@sial.com

Subscriptions

To request your FREE subscription to *Material Matters*, please contact us by:

Phone: 800-325-3010 (USA)
Mail: Attn: Marketing Communications
Aldrich Chemical Co., Inc.
Sigma-Aldrich Corporation
P.O. Box 2988
Milwaukee, WI 53201-2988
Website: sigma-aldrich.com/mm
Email: sams-usa@sial.com

International customers, please contact your local Sigma-Aldrich office. For worldwide contact information, please see back cover.

Material Matters is also available in PDF format on the Internet at sigma-aldrich.com/matsci.

Aldrich brand products are sold through Sigma-Aldrich, Inc. Sigma-Aldrich, Inc. warrants that its products conform to the information contained in this and other Sigma-Aldrich publications. Purchaser must determine the suitability of the product for its particular use. See reverse side of invoice or packing slip for additional terms and conditions of sale.

All prices are subject to change without notice.

Material Matters (ISSN 1933-9631) is a publication of Aldrich Chemical Co., Inc. Aldrich is a member of the Sigma-Aldrich Group. © 2010 Sigma-Aldrich Co.

"Your Materials Matter!"



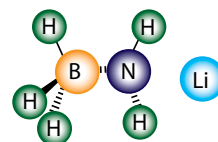
Joe Porwoll, President
Aldrich Chemical Co., Inc.

Do you have a compound that you wish Sigma-Aldrich® could list to help materials research? If it is needed to accelerate your research, it matters—please send your suggestion to matsci@sial.com and we will be happy to give it careful consideration.

Dr. Oleksandr Dolotko from ENSTA Paris Tech, France, suggested that we offer the newly developed Lithium Ammonia Borane (**Aldrich Prod. No. 710199**)¹ as a base material for alternative energy applications. This boron-based hydride is a low temperature source of hydrogen for fuel cells and other hydrogen consuming energy systems. Due to its distinct reactivity, Lithium Ammonia Borane can also serve as an excellent reducing agent in various chemical processes.²

References

- (1) Xiong, Z.; Yong, Ch. K.; Wu, G.; Chen, P.; Shaw, W.; Karkamkar, A.; Autrey, T.; Jones, M. O.; Johnson, S. R.; Edwards, P. P.; David, W. I. F. *Nature Materials* **2008**, 7, 138.
- (2) Myers, A. G.; Yang, B. H.; Kopecky, D. J. *Tetrahedron Let.* **1996**, 37, 3623.



Lithium ammonia borane, >90%

[99144-67-9] LiNH₂ · BH₃ FW 36.80

LiNH₂BH₃

| | |
|------------|------|
| 710199-1G | 1 g |
| 710199-10G | 10 g |

Nanomaterials Featured in this Issue

| Materials Category | Content | Page |
|---|---|------|
| Dyes and Ligands for Dye-sensitized Solar Cells | A selection of materials useful for organic photovoltaic devices | 39 |
| Nanopowders for Photovoltaic Applications | A list of high-purity nanopowders | 40 |
| Nanoparticle Dispersions | A list of nanoparticle dispersions | 40 |
| Electrode Materials for Lithium-ion Batteries | A list of Lithium containing materials for energy storage applications | 46 |
| Nanopowders for Energy Applications | A wide selection of nanopowders used for energy applications | 46 |
| Carbon Nanomaterials | A list of nanotubes, nanofibers and mesoporous nanomaterials | 47 |
| Titanate and Zirconate Nanopowders | A list of high-purity zirconate and titanate nanopowders | 54 |
| Other Titanate, Zirconate and Niobate Powders | A list of titanate, zirconate and niobate powders for electronic applications | 54 |

Synthesis of ZnO Aggregates and Their Application in Dye-sensitized Solar Cells



Qifeng Zhang, Kwangsuk Park, and Guozhong Cao*
 Materials Science and Engineering, University of Washington,
 Seattle, WA 98195, USA
 *Email: gzc@u.washington.edu

Introduction

Solar energy, as the primary source of energy for all living organisms on Earth, is considered the ultimate solution to the energy and environmental challenge as a carbon-neutral energy source. Many photovoltaic devices that fulfill the energy conversion from sunlight to electricity have already been developed over the past five decades. However, their widespread usage is still limited by two significant challenges; namely conversion efficiency and cost.¹ One of the more traditional photovoltaic devices, single crystalline silicon solar cells were invented more than 50 years ago, currently make up 94% of the market. Single crystalline silicon solar cells operate on the principle of p-n junctions formed by joining p-type and n-type semiconductors. The electrons and holes are photogenerated at the interface of p-n junctions, separated by an electrical field across the p-n junction, and collected through the external circuits. Unfortunately, single crystalline silicon solar cells suffer from both high materials costs and energy-intensive production processes. Amorphous thin film silicon is a good replacement candidate because the defect energy levels can be controlled by hydrogenation and the band gap can be reduced so that the light absorption efficiency can be much higher than that of crystalline silicon. However, amorphous silicon tends to be unstable and can lose up to 50% efficiency within the first one hundred hours. Bridging the gap between single crystalline silicon and amorphous silicon is the polycrystalline silicon film, for which a conversion efficiency of around 15% is obtained. Compound semiconductors such as gallium arsenide (GaAs, Aldrich Prod. No. 329010), cadmium telluride (CdTe, Aldrich Prod. No. 716669)

and copper indium gallium selenide (CIGS) have received much attention because they present a direct energy gap, can be doped to either p-type or n-type, have band gaps matching the solar spectrum, and possess high optical absorbance. These devices have demonstrated conversion efficiencies of 16-32%. Although photovoltaic devices built on silicon or compound semiconductors have been achieving high efficiency for practical use, they still require major breakthroughs to meet the long-term goal of very low cost (\$0.40/kWh).²⁻⁶

Dye-sensitized solar cells (DSCs) based on oxide semiconductors and organic dyes have recently emerged as a promising approach to efficient solar energy conversion at a low cost. The DSCs are a photoelectrochemical system which incorporates a porous-structured oxide film with adsorbed dye molecules as the photosensitized anode (Figure 1a and Figure 1b). A platinum-coated silicon wafer acts as the counter electrode (i.e., cathode), and a liquid electrolyte that traditionally contains I⁻/I₃⁻ redox couples serves as a conductor to electrically connect the two electrodes.⁷⁻¹² Photons are captured by the dye monolayer, creating excitons that are rapidly split at the nanocrystallite surface of oxide film; electrons are injected into the oxide film and holes are released by the redox couples in the liquid electrolyte. Compared with conventional single crystal silicon-based or compound semiconductor thin film solar cells, DSCs are thought to be advantageous as a photovoltaic device possessing both practical high efficiency and cost effectiveness. To date, the most successful DSC was based on a TiO₂ nanocrystalline film combined with ruthenium-polypyridine complex dye as first reported by O'Regan and Grätzel in 1991.¹³ A certified overall conversion efficiency of 11% was achieved on TiO₂-RuL'(NCS)₃ (namely "black dye") system, in which the spectral response of the complex dye was extended to the nearinfrared region so as to absorb far more of the incident light.^{9,14-16} The porous nature of nanocrystalline TiO₂ films drives their use in DSCs due to the high surface area available for dye molecule adsorption. Meanwhile, the suitable relative energy levels at the semiconductor-sensitizer interface, i.e., the position of the conduction band edge of TiO₂ being lower than the excited-state energy level of the dye, allow for the effective injection of electrons from the dye molecules to the semiconductor.

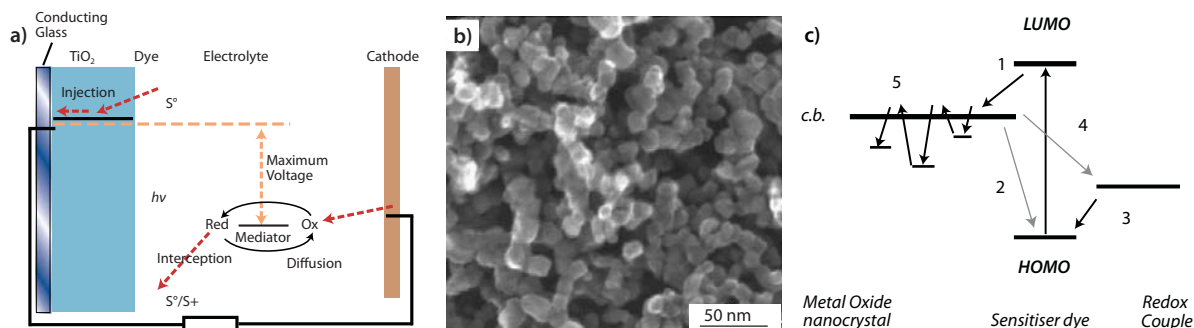


Figure 1. A dye-sensitized solar cell based on an electrochemical system. (a) Schematic of the construction and operational principle of device, (b) SEM image of oxide (TiO₂) electrode film with nanocrystallites (~20 nm in diameter), and (c) Electron transport in nanocrystalline oxide electrodes, in which photoexcited electrons are injected from the dye to the conduction band (denoted as "c.b.") of the nanocrystallite (1), the dye is regenerated by electron transfer from a redox couple in the electrolyte (3), a recombination may take place between the injected electrons and the dye cation (2) or redox couple (4). (4) is normally believed to be the predominant loss mechanism. Electron trapping in the nanocrystallites (5) is also a mechanism that causes energy loss. LUMO and HOMO represent the lowest unoccupied molecular orbital and the highest occupied molecular orbital of the dye, respectively.^{9,15,17}



The achievement of acceptable power conversion efficiencies instilled much confidence in the ability of DSCs to challenge the high costs of commercially available solar cells based on silicon or compound semiconductors. However, further increases in power conversion efficiency have been limited by the energy loss due to the recombination between electrons and either the oxidized dye molecules or electron accepting species in the electrolyte during the charge transport process (Figure 1c).¹⁸⁻²⁰ Such a recombination originates predominately from the lack of a depletion layer on TiO₂ nanocrystallite surface. This scenario becomes more evident when the thickness of photoelectrode film increases. A variety of approaches have been explored to overcome the electron recombination by using either one-dimensional nanostructures that provide a direct pathway for electron transport or using core-shell structures with an oxide coating on TiO₂ (Aldrich Prod. Nos. 718467, 677469) to minimize the recombination rate. Aside from those approaches, a series of methods that address the generation of photoexcited carriers by combining nanostructured films with optical effects (light scattering or optical confinement) has also been demonstrated to be effective in enhancing the light harvesting capability of the photoelectrode film so as to improve the DSC performance.²¹

Usami, Ferber, Luther, and Rothenberger et al. predicted that the optical absorption of dye sensitized TiO₂ nanocrystalline films could be enhanced by admixing large sized TiO₂ particles as the light scattering centers.²²⁻²⁴ The light scattering efficiency has been shown to correlate with both the size of the scattering centers and the wavelength of incident light.²⁵ The scattering reaches a maximum when the size of the scattering centers is about $k\lambda$, where k is a constant and λ is the wavelength. Experimentally, it has been verified that the performance of DSCs can be significantly improved when the TiO₂ nanocrystalline films are combined with large-sized SiO₂ (Aldrich Prod. No. 381276), Al₂O₃ (Aldrich Prod. No. 202606), or TiO₂ particles.²⁶⁻³⁰ By coupling a photonic crystal layer to conventional TiO₂ nanocrystalline films for light scattering, Nishimura et al. and Halaoui et al. also succeeded in enhancing the light harvesting capability of the photoelectrode.^{31,32} However, the introduction of large-sized particles into nanocrystalline films has the unavoidable effect of lowering the internal surface area of the photoelectrode film. This serves to counteract the enhancement effect of light scattering on the optical absorption, whereas the incorporation of a photonic crystal layer may lead to an undesirable increase in the electron diffusion length and, consequently, increase the recombination rate of photogenerated carriers.

Some recent developments have been reported on the use of oxide nanocrystallite aggregates in DSCs.³³⁻³⁷ The oxide nanocrystallite aggregates demonstrated to be able to provide the photoelectrode with both a large surface area and efficient light scattering centers. As a result, very impressive enhancements in the overall conversion efficiency were achieved for ZnO-based DSCs.^{33,36} This review introduces the synthesis, characterization, and surface modification of ZnO aggregates, and shows the light scattering effect with these aggregates on the enhancement of the light harvesting efficiency (LHE) of photoelectrode, resulting in a very impressive increase in the conversion efficiency of the DSCs.

Enhanced Solar Cell Performance with Aggregates

Synthesis of ZnO Aggregates

ZnO aggregates can be synthesized by the hydrolysis of a zinc salt in a polyol medium and heating at 160 °C.^{36,38} Typically, zinc acetate dihydrate (0.01 mol, Aldrich Prod. No. 379786) was added to diethylene glycol (DEG, 100 mL, Aldrich Prod. No. H26456) with vigorous stirring. The mixture was rapidly heated in an oil bath at a rate of 10 °C/min. The reaction continued for about 8 h with continual stirring. As-obtained colloidal solution was then sequentially concentrated by 1) centrifugally separating the aggregates from the solvent, 2) removing the supernatant, and 3) redispersing the precipitate in ethanol (5 mL). The sample synthesized at 160 °C is denoted as Sample 1. For comparison, three more samples were also synthesized at temperatures of 170, 180, and 190 °C, denoted as Samples 2 through 4, respectively.

Fabrication of Photoelectrode Films

Photoelectrode films were fabricated on Fluorine-Tin-Oxide (FTO) glass using a drop-casting method. After the films dried, they were annealed at 350 °C for 1 h to remove any residual organic matter from the ZnO surface. The films were then sensitized by immersing them into 0.5 mM ethanolic solution of the ruthenium complex *cis*-[Ru₂(NCS)₂] (commercially known as N3 dye, Aldrich Prod. No. 703206)^{39,40} for approximately 20 min. The sensitization time was controlled strictly and limited to avoid the dissolution of surface Zn atoms and the formation of Zn²⁺/dye complexes, which might block the electron transport from the dye to semiconductor. The films were then rinsed with ethanol to remove the additional dye.

Morphology and Structure Characterization

The morphology of the film of ZnO aggregates (Sample 1) was characterized using a scanning electron microscope (SEM), as shown in Figure 2. It can be seen that the film is well-stacked with submicrometer-sized ZnO aggregates. These aggregates are polydisperse in size with diameters ranging from several tens to several hundreds of nanometers. The film therefore presents a highly disordered structure.

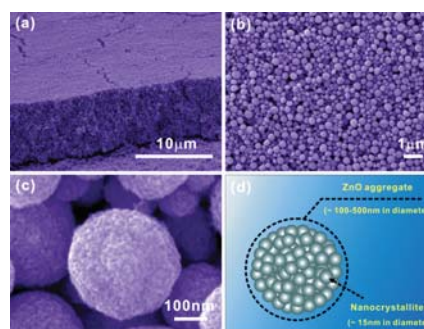


Figure 2. SEM images of ZnO film with aggregates synthesized at 160 °C (Sample 1) and a schematic showing the structure of individual aggregates.

A high magnification SEM image reveals that the ZnO aggregate is nearly spherical in shape and consists of packed nanocrystallites. In Figure 2d, the structure of an individual aggregate is schematically illustrated to further demonstrate the porous features provided due to the agglomeration of nanosized crystallites. This ZnO film was thought to adopt as a hierarchical structure in view of the architecture formed by secondary submicron-sized aggregates with primary nanocrystallites.

Shown in **Figure 3** are the SEM images of Samples 2 through 4. It is clear that, with increasing synthesis temperature, the degree of a spherical agglomeration of the nanocrystallites is gradually degraded. Sample 2, synthesized at 170 °C, is similar to Sample 1 and consists of aggregated ZnO nanocrystallites, but begins to show a slight destruction of the spherical shape (**Figure 3a**). Sample 3, synthesized at 180 °C, consists of partial aggregates, however most of the aggregates have lost their spherical shape (**Figure 3b**). As the synthesis temperature increases further to 190 °C, the obtained product (Sample 4) only presents dispersed nanocrystallites without any agglomeration (**Figure 3c**). X-ray diffraction (XRD) analysis revealed that all the samples were of a hexagonal wurtzite structure of ZnO. With XRD spectra and using the Scherrer equation,⁴¹ the primary nanocrystallite size was estimated to be about 15 nm in diameter for all the samples, i.e., there was no appreciable difference in the nanocrystallite size for these samples, despite the differences in synthesis temperature and morphology. Nitrogen sorption isotherms revealed that all four samples possessed almost equal specific surface area of approximately 80 m²/g.

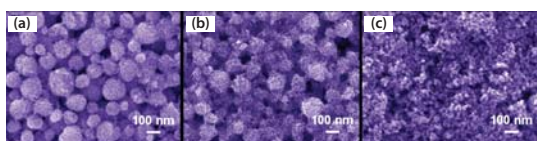


Figure 3. SEM images of ZnO films with synthesis temperature of 170, 180, and 190 °C, corresponding to Samples 2 through 4, respectively.

Light Scattering of ZnO Aggregate Films

It was observed that Samples 1 through 4, i.e., the ZnO films synthesized at different temperatures as SEM images shown in **Figures 2 and 3**, demonstrated a difference in their transparency. This was a result of light scattering, as observed in the optical absorption spectra of the films upon dye sensitization (**Figure 4**). In the spectra, all the samples exhibit an intrinsic absorption with similar absorption intensity below 390 nm, caused by the ZnO semiconductor owing to electron transfer from the valence band to the conduction band. However, absorption at wavelengths above 400 nm vary significantly; such absorption originates from the dye molecules adsorbed on the ZnO surface and is related to the film structure. It has the highest intensity for Sample 1, less intensity for Samples 2 and 3, and the lowest intensity for Sample 4. It should be noted that only Sample 4 presents an absorption peak centered around 520 nm, corresponding to the visible $t_2 \rightarrow \pi^*$ metal-to-ligand charge transfer (MLCT)³⁹ in N3 dye but with a slight blue-shift due to the electronic coupling between N3 and ZnO, whereas the other three samples (1–3) show a monotonically increased absorption as the wavelength switches from visible to ultraviolet. The absorption spectra illustrate that the better aggregation of nanocrystallites induces more effective photon capturing in the visible region and also suggest the existence of a strong light scattering effect. Such an effect may partially scatter the incident light and weaken the transmittance of the films, thus resulting in the pseudo absorption deviating from that of adsorbed dye.

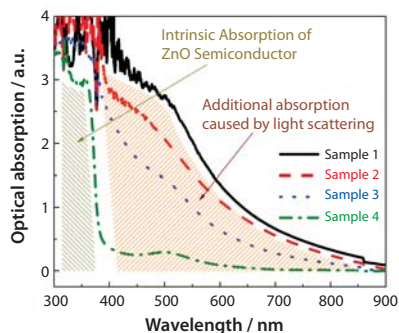


Figure 4. Optical absorption spectra of ZnO films of Samples 1 through 4.

Mie theory^{42,43} and Anderson localization of light⁴⁴ provide the analytical description for the scattering of light by spherical particles and predict that resonant scattering may occur when the particle size is comparable to the wavelength of incident light. The aggregates within ZnO films are submicrometer-sized, and they are therefore particularly efficient scatterers for visible light, resulting in a significant increase in the light harvesting capability of the photoelectrode. Unlike large oxide particles, the ZnO aggregates are closely packed with nanocrystallites and therefore do not cause any loss in the internal surface area. It should be noted that the light scattering effect is usually imperceptible in conventional mesoporous TiO₂ electrodes consisting of nanocrystallites smaller than 50 nm, because the size is far away from the wavelength of visible light; this is also the reason why Sample 4 presents a relatively weak absorption at the visible wavelengths.

Solar Cell Performance

The solar cells with as-prepared ZnO films were characterized by measuring the current–voltage behavior while irradiated by simulated AM 1.5 sunlight with a power density of 100 mW/cm². **Figure 5** shows typical current density versus voltage curves of the four ZnO samples. Sample 1, with near perfect aggregation, achieved the highest short-circuit current density and, thus, the highest conversion efficiency, whereas Sample 4, consisting of only ZnO nanocrystallites, presented the lowest current density and the lowest energy conversion efficiency of all four samples. **Table 1** summarizes the open-circuit voltages, the short-circuit current densities, the fill factors, and the overall energy conversion efficiencies for all four samples. All samples possessed the same or similar open-circuit voltages of approximately 600 mV; however, the short-circuit current density varied significantly from 19 mA/cm² for Sample 1 to 10 mA/cm² for Sample 4. As a result, the energy conversion efficiency varied systematically from 5.4% for Sample 1 to 2.4% for Sample 4, decreasing as the degree of spherical aggregation decreased.

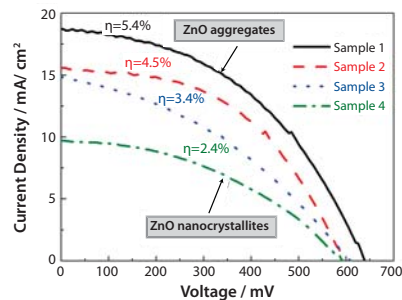


Figure 5. Photovoltaic response of ZnO films, Samples 1 through 4, while irradiated by standard AM 1.5 sunlight with an output power of 100 mW/cm².

Table 1. Photovoltaic Properties of Dye-sensitized ZnO Solar Cells

| Sample | V _{oc} (mV) | I _{sc} (mAcm ⁻²) | FF[%]* | η[%]* |
|--------|----------------------|---------------------------------------|--------|-------|
| 1 | 635 | 18.7 | 45.1 | 5.4 |
| 2 | 595 | 15.6 | 48.7 | 4.5 |
| 3 | 605 | 14.9 | 37.8 | 3.4 |
| 4 | 595 | 9.7 | 41.1 | 2.4 |

*The conversion efficiency η and fill factor FF are calculated from $\eta = P_{out,max}/P_{in}$ and $FF = P_{out,max}/(V_{oc} \times I_{sc})$, where $P_{out,max}$ is the maximum output power density, P_{in} is power density of the incident light, V_{oc} is the open-circuit voltage, and I_{sc} is the short-circuit current.

In view of the different optical absorption of these films, the variation in the solar cell conversion efficiency could be attributed to light scattering caused by a disordered film structure formed by the polydisperse aggregates. A disordered structure may lead to random multiple scattering in the film and, possibly, result in light localization due to the formation of traps for optical confinement. Photoinduced lasing emission on closely packed ZnO cluster films reported by Cao et al.⁴⁵ and Wu et al.⁴⁶ is one example that manifests the light scattering effect



of highly disordered structure on the generation of light localization. In ZnO solar cells that consist of a photoelectrode film with aggregates, the light scattering may significantly extend the traveling distance of light within the photoelectrode and, thus, increase the probability of interaction between the photons and dye molecules. That means, the light scattering may result in an enhancement in the LHE of photoelectrode and therefore increases the conversion efficiency of solar cells. This is the reason that, in **Figure 5**, Sample 1 achieves a conversion efficiency of 5.4%, much higher than 2.4% obtained for Sample 4, the ZnO nanocrystalline film without light scattering.

Size Dependence of Conversion Efficiency

Size dependence of the solar cell conversion efficiency has been investigated to further demonstrate that the light scattering effect is closely related to the structure of the photoelectrode film, such as the average size and size distribution of the aggregates. For this purpose, both monodisperse and polydisperse ZnO aggregates were prepared. The method for the synthesis of polydisperse ZnO aggregates is a polyol-mediated precipitation method similar to that described above; however, the rate of heating was adopted to be different to control the degree of polydispersity. Specifically, a rapid heating at 10 °C/min was used to fabricate the polydisperse ZnO aggregates with a broad size distribution, while a rate of 5 °C/min was used to obtain the polydisperse aggregates with the relatively narrow size distribution. To synthesize monodisperse ZnO aggregates, an amount of stock solution was added into the reaction solution when the temperature reached 130 °C while the zinc acetate was completely dissolved. The stock solution was made of 5 nm ZnO nanoparticles prepared via a sol-gel approach and dispersed in the diethylene glycol with a concentration of about 10^{-3} M. The size of the aggregates could be adjusted by the amount of stock solution used. For example, 0.5 mL, 1 mL, 5 mL, 10 mL and 20 mL of stock solution gave monodisperse ZnO aggregates of 350 nm, 300 nm, 250 nm, 210 nm and 160 nm in diameter, respectively.

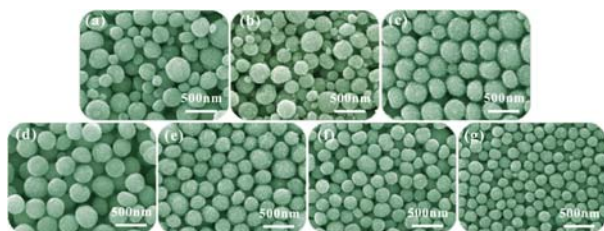


Figure 6. SEM images of ZnO films with aggregates different in size and size distribution. (a) and (b) Polydisperse aggregates, corresponding to groups 1 and 2, respectively, and (c) through (g) monodisperse aggregates, corresponding to groups 3 through 7, respectively.

To study the effects of the average size and size distribution of the aggregates on the solar-cell performance, a number of ZnO films with various structures were prepared and classified into seven groups, named group 1, 2, . . . through 7, in which the films in groups 1 and 2 were made of polydisperse ZnO aggregates and the others only included monodisperse aggregates. **Figure 6** shows typical SEM images of all these film samples, where **Figure 6a** through **6g** corresponds to the samples that belong to groups 1 through 7, respectively. One can see that the samples in group 1 consisted of polydisperse ZnO aggregates with diameter varying from 120 to 360 nm, while the samples in group 2 also consisted of polydisperse ZnO aggregates but with the diameter in the region of ~120–310 nm. The other samples were all monodisperse ZnO aggregates with average sizes varying from ~350 nm for group 3, ~300 nm for group 4, ~250 nm for group 5, ~210 nm for group 6, to ~160 nm for group 7.

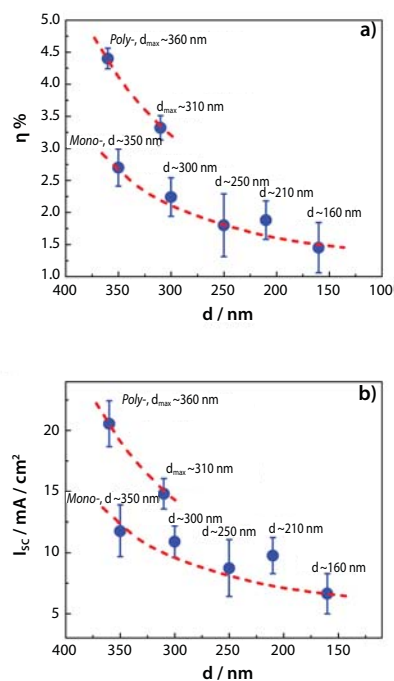


Figure 7. Dependence of (a) overall energy-conversion efficiency and (b) short-circuit current density on the size and size distribution of aggregates in dye-sensitized ZnO solar cells.

The solar-cell performance was characterized by measuring the current-voltage (I–V) behaviors of all of the samples when irradiated by a simulated AM 1.5 sunlight with a power density of 100 mW/cm². The results are summarized in **Figure 7**, where **Figure 7a** shows the dependence of the energy-conversion efficiency on the diameter and size distribution of the ZnO aggregates, and **Figure 7b** indicates a similar trend for the short-circuit current density. It is clear that the photoelectrode films with polydisperse ZnO aggregates have both a higher energy-conversion efficiency and a larger short-circuit current density than the films with monodisperse ZnO aggregates. The electrode films consisting of polydisperse ZnO aggregates with a maximum diameter of 360 nm (samples in group 1) present the highest conversion efficiency of all the samples (4.4%), 33% higher than the efficiency of the polydisperse ZnO aggregates (3.3%) with the maximum diameter of 310 nm (samples in group 2), and 63% higher than the efficiency of monodisperse ZnO aggregates (2.7%) with an average size of ~350 nm (samples in group 3). Similarly, the largest short circuit current density of 21 mA/cm², achieved for the polydisperse ZnO aggregates with the maximum diameter of 360 nm (samples in group 1), is 40% higher than that of 15 mA/cm² for the polydisperse ZnO aggregates with the maximum diameter of 310 nm (samples in group 2), and 75% higher than that of 12 mA/cm² for the monodisperse ZnO aggregate films (samples in group 3). As for the ZnO films with only monodisperse aggregates, one can see that the decrease in the size of the ZnO aggregates directly results in the degradation of the short-circuit current density from 12 mA/cm² to 7 mA/cm² and the energy-conversion efficiency from 2.7% to 1.5%. It has been demonstrated that the variation of conversion efficiency for the ZnO solar cell samples in different groups only results from the difference in photocurrent of the cells instead of open-circuit voltage or fill factor. Moreover, the photocurrent was basically related to either the dye adsorption amount determined by the internal surface area of the photoelectrode film or the propagation behavior of light within the photoelectrode film. A nitrogen sorption isotherm measurement revealed a same specific surface area, ~80 m²/g, for all these samples in different groups. The dye adsorption amount was probably not the reason for the difference in the short-

circuit current density. Therefore, it was inferred that the film structures with differences in the aggregate size and size distribution might have different impacts on the transport of light so that the LHE of the photoelectrode was significantly affected.

To demonstrate the impact of film structure on the transport of light, optical absorption spectra of all the films in seven groups were measured, as shown in Figure 8. The film with 160 nm diameter ZnO nanocrystallites presented a typical absorption like that obtained for single crystalline ZnO. The absorption below 385 nm, corresponding to the band gap energy of 3.2 eV, represents the intrinsic optical absorption of ZnO semiconductor caused by the electron transit from the valence band to the conduction band. Almost no absorption can be observed from this film in the visible region with wavelength above 385 nm. As the ZnO aggregates of nanocrystallites are gradually formed and the aggregate size increases, the optical absorption of films in the visible region is apparently increased. The most significant increase occurs on the film that belongs to group 1, consisting of polydisperse ZnO aggregates with a broad size distribution from 120 to 360 nm in diameter. The result implies that the enhancement in optical absorption originates from the aggregation of ZnO nanocrystallites and is proportional to the average size of mono-sized aggregates or the dispersion degree of polydisperse aggregates in size distribution. This phenomenon can be explained by the light scattering of submicron-sized ZnO aggregates, which may change the transport direction of light travelled in the films and hereby attenuate the light that transmits through the films.

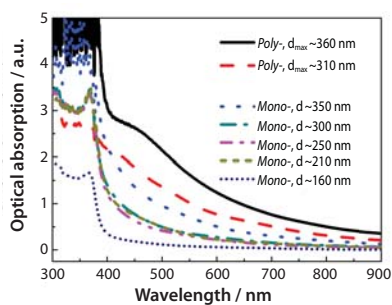


Figure 8. Optical absorption spectra of ZnO films consisting of aggregates with different sizes and size distributions.

The light scattering influences the transport behavior of light by changing the path and/or extending the distance of light travelled within the photoelectrode film, and thus the light harvesting efficiency improves due to the increased probability of interaction between the photons and the dye molecules that adsorb on the ZnO nanocrystallites. Compared with the films that contain only mono-dispersed aggregates, the films with polydisperse aggregates present an apparent virtue in the enhancement of optical absorption and energy conversion efficiency, as shown in Figure 8 and Figure 7a, respectively. Polydisperse aggregates likely lead to disordered structure when they are packed in a random way to form the film. Literature has demonstrated that the less ordered medium is more effective in the generation of multiple scattering to light and the formation of closed loops for light confinement.⁴⁵⁻⁴⁷ The broader distribution of aggregate size means the increased irregularity in the assembly of film, resulting in the fact that the samples in group 1 consisting of polydisperse aggregates with the size distribution in a quite large range possess the highest conversion efficiency. Another reason that polydisperse aggregates exhibit excellent ability to enhance optical absorption and solar cell efficiency is that the different sized aggregates can cause light scattering in a wide wavelength range. Besides the effect to generate strong light scattering, polydisperse aggregates are also thought to be good at the formation of network interconnection so as to create the photoelectrode film with a closely-packed structure, which offers more pathways for the transport of electrons in the film.

Surface Modification Leading to Higher Conversion Efficiencies

Lithium Ion-Mediated Growth of ZnO Aggregates

Lithium ions have been reported to be able to mediate the growth of the ZnO aggregates, leading to an increase in the nanocrystallite size and a polydisperse distribution in the size of the aggregates. This impacts the photoelectrode film with improved dye adsorption and more effective light scattering, and thus enhances the performance of DSCs with an almost 53% increase in the conversion efficiency. The improvement in solar cell performance started with the synthesis of ZnO aggregates in the presence of lithium ions. For a typical fabrication process, 0.1 M zinc acetate dihydrate ($\text{ZnAc} \cdot 2\text{H}_2\text{O}$) and 0.01 M lithium acetate salt (e.g., $\text{LiAc} \cdot 2\text{H}_2\text{O}$, Aldrich Prod. No. 450189) were added to diethylene glycol (DEG) and the mixture was heated to 160 °C at a rate of 5 °C/min. The solution was kept at 160 °C for about 2 h so as to allow for the necessary chemical reactions to occur. Similar to the treatment for preparing pure ZnO aggregates, the colloid was then concentrated by a sequential treatment of centrifugation, removal of the supernatant, and several redispersals of the precipitate in ethanol. The precipitate was finally dispersed in ethanol with a concentration of approximately 0.5 M and as-obtained colloidal suspension solution was ready for making photoelectrode film. The ZnO aggregates synthesized in the presence of lithium ions was denoted as 'Li-ZnO'. For comparison, 'pure-ZnO' aggregate films were also prepared as reference while the reaction solution only contained $\text{ZnAc} \cdot 2\text{H}_2\text{O}$ and DEG.

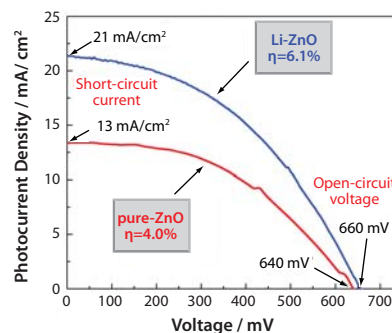


Figure 9. Photovoltaic behavior of ZnO films consisting of aggregates synthesized in the presence (denoted as 'Li-ZnO') and absence (denoted as 'pure-ZnO') of lithium salt.

Figure 9 shows the typical photovoltaic behavior of ZnO films consisting of aggregates synthesized in the presence and absence of lithium ions. These two types of films display similar open-circuit voltages (V_{oc}) in the range of 640–660 mV and fill factors (FF) of 0.44–0.48. However, they differ in short-circuit photocurrent densities (I_{sc}), i.e., 13 mA/cm² for pure-ZnO and 21 mA/cm² for Li-ZnO. The larger photocurrent density leads to higher conversion efficiency. The efficiency of the Li-ZnO film reached 6.1%, while a value of 4.0% was attained for the pure-ZnO film. Such a significant enhancement in the conversion efficiency was ascribed to the use of lithium ions during the ZnO aggregate synthesis, which offered a positive influence on the solar cell performance by affecting the morphology, structure, and surface chemistry of the aggregates, and thus resulted in increased dye adsorption and more effective light scattering.

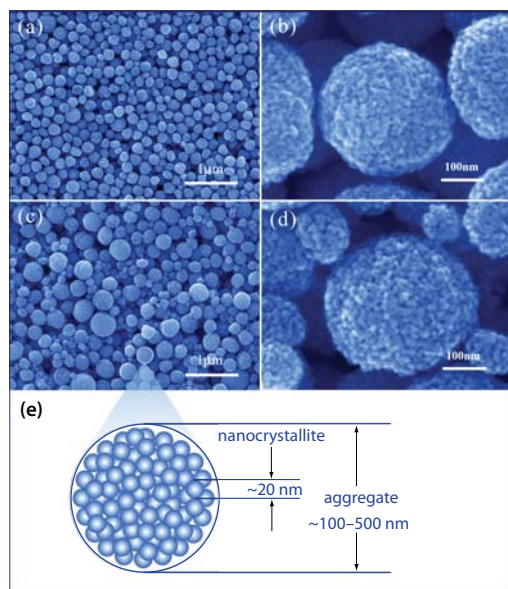


Figure 10. Morphology and structure of ZnO aggregate films. Images (a) and (b) are SEM images with different magnifications for the pure-ZnO film. Images (c) and (d) are SEM images of the Li-ZnO film, and (e) is a drawing to illustrate the hierarchical structure of the aggregates consisting of ZnO nanocrystallites.

Shown in **Figure 10** are the SEM images of pure-ZnO and Li-ZnO films. An apparent difference in the morphology can be seen under low magnification (**Figure 10a** and **Figure 10c**). The pure-ZnO film is comprised of aggregates with a monodisperse size distribution, whereas the Li-ZnO film exhibits a broad distribution of aggregate size from several tens to several hundreds of nanometers. The different polydispersity of ZnO aggregates synthesized in the presence of lithium salt reflects the important influence of lithium ions on the growth of ZnO aggregates. It is possible that these lithium ions adsorb on the ZnO surface so as to mediate the agglomeration of ZnO nanocrystallites. A polydisperse size distribution of Li-ZnO aggregates is beneficial to light scattering, and it was thought to contribute to the light harvesting efficiency of the photoelectrode and partially resulted in an increase in the conversion efficiency of the cells. The difference of pure-ZnO and Li-ZnO films in the light scattering ability was confirmed by measuring optical absorption spectra of these two films. The results are shown in **Figure 11**. It can be seen that both films present an intrinsic absorption band at wavelengths below 385 nm and an additional absorption hump in the visible region. The latter is thought to be a result of light scattering, which causes light extinction via diffuse reflection and/or diffuse transmission. This affects the film transparency and appears in the spectra as pseudo-absorption. For the Li-ZnO film, it shows that the absorption in the visible region is stronger than that of the pure-ZnO. This is just because the aggregates in the Li-ZnO film are highly polydisperse in size and may generate more efficient light scattering than the monodisperse aggregates.

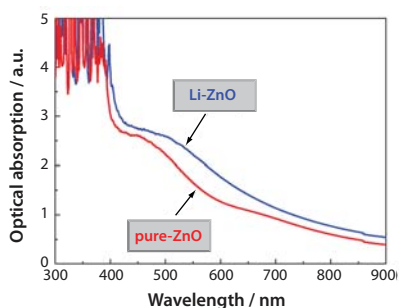


Figure 11. Optical absorption spectra of pure ZnO and Li-ZnO films.

Besides enhanced light scattering effect due to the polydispersity of ZnO aggregates in size, the use of lithium ions in the synthesis was also mentioned to increase the nanocrystallite size of ZnO and the pore size of aggregates. This offered a more porous structure for dye infiltration and electrolyte diffusion. Furthermore, the presence of lithium ions might also enhance the surface stability of ZnO, which would prevent the formation of Zn²⁺/dye complexes and favor dye adsorption on ZnO in a monolayer. All these factors were thought to be helpful to improving the solar cell performance. It is worth noting that these samples were characterized through X-ray photoelectron spectroscopy (XPS). No detectable difference could be found in the XPS spectra for the pure-ZnO and Li-ZnO films, indicating that these two films are identical with regards to chemical composition. In other words, it excludes the possibility that lithium exists in the ZnO as a dopant or forms a composite with ZnO, although the term "Li-ZnO" is used to represent the ZnO aggregates that are synthesized in the presence of lithium ions.

Atomic Layer Deposition of TiO₂ on ZnO Surface

Besides lithium ions that may mediate the growth and thus change the surface of the ZnO aggregates, another way to improve the surface stability of ZnO aggregates in a ruthenium complex dye is to deposit a thin film on the ZnO surface to form a core/shell structure.⁴⁸ Atomic layer deposition (ALD) is an ideal technique for creating the core/shell structure due to its unique self-limiting nature and low growth temperature, which make it possible to apply an ultra-thin layer on porous structures.^{49,50} When ALD technique was employed to deposit an ultra-thin TiO₂ layer on the porous ZnO aggregates, it significantly enhanced conversion efficiency of the solar cells. As illustrated schematically in **Figures 12a-c**, TiO₂ ultra-thin layer deposited by ALD shows complete and conformal coverage on the surface and inside the pores of the aggregates. All of the dye molecules are adsorbed onto the surface of TiO₂ coating. Such an ultra-thin and conformal ALD coating is so thin that it does not change the morphology of the underlying ZnO structures as shown in **Figure 12e** and **Figure 12f**. It was estimated that the thickness of the TiO₂ coating layer after 10 cycles of ALD is 0.3–0.6 nm.^{51,52} The connections between adjacent ZnO nanocrystallites would remain to ensure a favorable electron motion through ZnO (as suggested in **Figure 12d**). Such a feature in the structure would improve the surface stability of the ZnO aggregates with enhanced dye loading, while retaining the advantage of high electron mobility of ZnO.

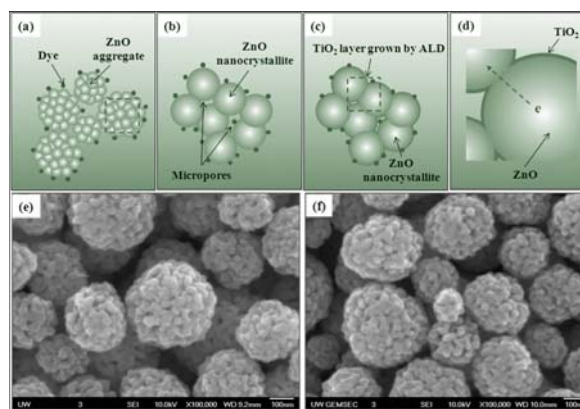


Figure 12. Schematics illustrating (a) ZnO aggregates adsorbed with dye molecules, (b) ZnO nanocrystallites containing micropores, (c) conformal ALD-TiO₂ thin layer on the surface of ZnO nanocrystallites, (d) enlarged schematic showing the details of conformal ALD-TiO₂ coating on ZnO surface and the uninterrupted connection between adjacent ZnO nanocrystallites for efficient electron motion, and SEM images of photoelectrode films of (e) submicron-sized aggregates of ZnO nanocrystallites and (f) submicron-sized aggregates of ZnO nanocrystallites coated with thin TiO₂ layer.

A Brunauer-Emmett-Teller (BET)⁵³ characterization of the TiO₂-coated ZnO aggregates implies that micropores inside each aggregate still remain after the ALD treatment, indicating that the porous structure of the photoelectrode film is preserved. This is very important for the photoelectrode to achieve sufficient dye adsorption. Due to the introduction of TiO₂ coating layer, a slight decrease in both the size and the volume of the micropores was observed. It was thought that the structure of ZnO aggregates with a TiO₂ coating layer was able to suppress the recombination because of the formation of a n-n* heterojunction at the ZnO/TiO₂ interface.⁵⁴ This could be verified by the electrochemical impedance spectroscopy (EIS), which showed the suppressed recombination at the aggregate/electrolyte interface due to the coating of TiO₂ layer. As a result, both the open circuit voltage and the fill factor of the cell were increased and, impressively, the conversion efficiency was improved from 5.2% to 6.3% (Table 2).⁵⁵

Table 2. Performance of the Solar Cells with the Electrode Made of ZnO and TiO₂ Coated ZnO Films

| Sample | V _{oc} [mV] | I _{sc} [mAcm ⁻²] | FF | η[%] |
|-----------------------------|----------------------|---------------------------------------|------|------|
| ZnO | 65.8 | 16.3 | 0.48 | 5.2 |
| TiO ₂ coated ZnO | 70.9 | 15.8 | 0.56 | 6.3 |

Conclusions

ZnO aggregates were synthesized and studied as a photoelectrode material in DSCs. Such aggregates are formed by nano-sized crystallites, and thus possess extremely large surface areas. Simultaneously, the size of the aggregates is in the submicron range; which is comparable to the wavelength of the visible light and, therefore, the aggregates are very effective in light scattering. The existence of light scattering in a photoelectrode film may significantly extend the traveling distance of the light and as such enhance the light harvesting efficiency of the photoelectrode. This finally leads to an improvement in the conversion efficiency of a DSC with photoelectrode consisting of the aggregates. Typically, in the case of ZnO, the aggregates have presented an increase in the conversion efficiency of more than 120% compared with nanocrystallites, which are far smaller than the light wavelength in size and unable to generate light scattering.

A polydisperse distribution in the aggregate size might facilitate the generation of more intensive light scattering. The use of lithium ions to mediate the growth of the ZnO aggregates resulted in a polydisperse distribution and an improved surface stability of the ZnO in the ruthenium complex dye. The treatment of the ZnO aggregate film with an ALD technique for coating a TiO₂ layer proved to be helpful in reducing the electron recombination due to the formation of a n-n* heterojunction at the ZnO/TiO₂ interface. Both these surface modification methods have been verified to result in an increase in the conversion efficiency of the dye-sensitized ZnO aggregate solar cells from 5.2-5.4% to 6.2-6.3%. The use of nanocrystallite aggregates in the photoelectrode film for light scattering is anticipated to further improve the performance of DSCs based on TiO₂, which have already achieved 10-11% conversion efficiencies.

Acknowledgments

This work is supported by the U.S. Department of Energy, Office of Basic Energy Sciences, Division of Materials and Engineering under Award No. DE-FG02-07ER46467 (Q.F.Z.), the Air Force Office of Scientific Research (AFOSR-MURI, FA9550-06-1-0326) (K.S.P.), the University of Washington TGIF grant, the Washington Research Foundation, and the Intel Corporation.

References

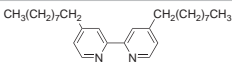
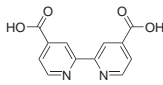
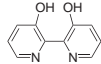
- Liu, J.; Cao, G. Z.; Yang, Z. G.; Wang, D. H.; Dubois, D.; Zhou, X. D.; Graff, G. L.; Pederson, L. R.; Zhang, J. G. *ChemSusChem* **2008**, *1*, 676.
- Carlson, D. E.; Wronski, C. R. *Appl. Phys. Lett.* **1976**, *28*, 671.
- Chopra, K. L.; Paulson, P. D.; Dutta, V. *Prog. Photovoltaics* **2004**, *12*, 69.
- Goetzberger, A.; Hebling, C. *Sol. Energy Mater. Sol. Cells* **2000**, *62*, 1.
- Goetzberger, A.; Hebling, C.; Schock, H. W. *Mater. Sci. Eng., R* **2003**, *40*, 1.
- Ward, J. S.; Ramanathan, K.; Hasoon, F. S.; Coutts, T. J.; Keane, J.; Contreras, M. A.; Moriarty, T.; Noufi, R. *Prog. Photovoltaics* **2002**, *10*, 41.
- Bisquert, J.; Cahen, D.; Hodes, G.; Zaban, A. *J. Phys. Chem. B* **2004**, *108*, 8106.
- Grätzel, M. *Prog. Photovoltaics* **2000**, *8*, 171.
- Grätzel, M. *Nature* **2001**, *414*, 338.
- Kroon, J. M.; Bakker, N. J.; Smit, H. J. P.; Liska, P.; Thampij, K. R.; Wang, P.; Zakeeruddin, S. M.; Grätzel, M.; Hinsch, A.; Hore, S.; Würfel, U.; Sastrawan, R.; Durrant, J. R.; Palomares, E.; Pettersson, H.; Gruszecki, T.; Walter, J.; Skupien, K.; Tulloch, G. E. *Prog. Photovoltaics* **2007**, *15*, 1.
- Longo, C.; De Paoli, M. A. *J. Braz. Chem. Soc.* **2003**, *14*, 889.
- Martinson, A. B. F.; Hamann, T. W.; Pellin, M. J.; Hupp, J. T. *Chem. Eur. A* **2008**, *14*, 4458.
- O'Regan, B.; Grätzel, M. *Nature* **1991**, *353*, 737.
- Grätzel, M. *J. Photochem. Photobiol., C* **2003**, *4*, 145.
- Grätzel, M. *Philos. Trans. R. Soc. London, Ser. A* **2007**, *365*, 993.
- Nazeeruddin, M. K.; Pechy, P.; Renouard, T.; Zakeeruddin, S. M.; Humphry-Baker, R.; Comte, P.; Liska, P.; Cevey, L.; Costa, E.; Shklover, V.; Spiccia, L.; Deacon, G. B.; Bignozzi, C. A.; Grätzel, M. *J. Am. Chem. Soc.* **2001**, *123*, 1613.
- Nelson, J.; Chandler, R. E. *Coord. Chem. Rev.* **2004**, *248*, 1181.
- Grätzel, M. *J. Photochem. Photobiol., A* **2004**, *164*, 3.
- Grätzel, M. *Inorganic Chemistry* **2005**, *44*, 6841.
- Nissfolk, J.; Fredin, K.; Hagfeldt, A.; Boschloo, G. *J. Phys. Chem. B* **2006**, *110*, 17715.
- Rockstuhl, C.; Lederer, F.; Bittkau, K.; Carius, R. *Appl. Phys. Lett.* **2007**, *91*, 171104.
- Ferber, J.; Luther, J. *Sol. Energy Mater. Sol. Cells* **1998**, *54*, 265.
- Rothenberger, G.; Comte, P.; Grätzel, M. *Sol. Energy Mater. Sol. Cells* **1999**, *58*, 321.
- Usami, A. *Chem. Phys. Lett.* **1997**, *277*, 105.
- Koo, H. J.; Park, J.; Yoo, B.; Yoo, K.; Kim, K.; Park, N. G. *Inorg. Chim. Acta* **2008**, *361*, 677.
- Anderson, C.; Bard, A. J. *J. Phys. Chem. B* **1997**, *101*, 2611.
- Barbe, C. J.; Arendse, F.; Comte, P.; Jirousek, M.; Lenzmann, F.; Shklover, V.; Grätzel, M. *J. Am. Chem. Soc.* **1997**, *80*, 3157.
- Hore, S.; Nitz, P.; Vetter, C.; Prah, C.; Niggemann, M.; Kern, R. *Chem. Commun.* **2005**, 2011.
- So, W. W.; Kim, K. J.; Lee, J. K.; Moon, S. J. *Jpn. J. Appl. Phys., Part 1* **2004**, *43*, 1231.
- Yang, L.; Lin, Y.; Jia, J. G.; Xiao, X. R.; Li, X. P.; Zhou, X. W. *J. Power Sources* **2008**, *182*, 370.
- Halaoui, L. I.; Abrams, N. M.; Mallouk, T. E. *J. Phys. Chem. B* **2005**, *109*, 6334.
- Nishimura, S.; Abrams, N.; Lewis, B. A.; Halaoui, L. I.; Mallouk, T. E.; Benkstein, K. D.; van de Lagemaat, J.; Frank, A. J. *J. Am. Chem. Soc.* **2003**, *125*, 6306.
- Cao, G. Z. *Photonics Spectra* **2008**, *42*, 60.
- Chou, T. P.; Zhang, Q. F.; Fryxell, G. E.; Cao, G. Z. *Adv. Mater.* **2007**, *19*, 2588.
- Zhang, Q. F.; Chou, T. P.; Russo, B.; Jenekhe, S. A.; Cao, G. *Adv. Funct. Mater.* **2008**, *18*, 1654.
- Zhang, Q. F.; Chou, T. R.; Russo, B.; Jenekhe, S. A.; Cao, G. Z. *Angew. Chem. Int. Ed.* **2008**, *47*, 2402.
- Zhang, Q. F.; Dandeneau, C. S.; Zhou, X. Y.; Cao, G. Z. *Adv. Mater.* **2009**, *21*, 4087.
- Jezequel, D.; Guenot, J.; Jouini, N.; Fievet, F. *J. Mater. Res.* **1995**, *10*, 77.
- Nazeeruddin, M. K.; Kay, A.; Rodicio, I.; Humphrybaker, R.; Muller, E.; Liska, P.; Vlachopoulos, N.; Grätzel, M. *J. Am. Chem. Soc.* **1993**, *115*, 6382.
- Ryan, M. *Platinum Met. Rev.* **2009**, *53*, 216.
- Guinier, A. *X-ray Diffraction in Crystals, Imperfect Crystals, and Amorphous Bodies*; Dover Publications: Mineola, New York, 1994.
- Barber, P.; Hill, S. *Light Scattering by Particles: Computational Methods*; World Scientific Pub Co Inc: Singapore, 1990.
- Hulst, H. *Light Scattering by Small Particles*; Dover Pubs: Mineola, New York, 1981.
- Wolf, P. E.; Maret, G. *Phys. Rev. Lett.* **1985**, *55*, 2696.
- Cao, H.; Xu, J. Y.; Zhang, D. Z.; Chang, S. H.; Ho, S. T.; Seelig, E. W.; Liu, X.; Chang, R. P. H. *Phys. Rev. Lett.* **2000**, *84*, 5584.

- (46) Wu, X. H.; Yamilov, A.; Noh, H.; Cao, H.; Seelig, E. W.; Chang, R. P. H. *J. Opt. Soc. Am. B: Opt. Phys.* **2004**, *21*, 159.
- (47) Wiersma, D. S.; Bartolini, P.; Lagendijk, A.; Righini, R. *Nature* **1997**, *390*, 671.
- (48) Diamant, Y.; Chappel, S.; Chen, S. G.; Melamed, O.; Zaban, A. *Coord. Chem. Rev.* **2004**, *248*, 1271.
- (49) Knez, M.; Niesch, K.; Niinisto, L. *Adv. Mater.* **2007**, *19*, 3425.
- (50) Rosental, A.; Tarre, A.; Gerst, A.; Uustare, T.; Sammelselg, V. *Sens. Actuators, B* **2001**, *77*, 297.
- (51) Aarik, J.; Aidla, A.; Uustare, T.; Ritala, M.; Leskela, M. *Appl. Surf. Sci.* **2000**, *161*, 385.
- (52) Hamann, T. W.; Martinson, A. B. F.; Elam, J. W.; Pellin, M. J.; Hupp, J. T. *J. Phys. Chem. C* **2008**, *112*, 10303.
- (53) Brunauer, S.; Emmett, P. H.; Teller, E. *J. Am. Chem. Soc.* **1938**, *60*, 309.
- (54) Law, M.; Greene, L. E.; Radenovic, A.; Kuykendall, T.; Liphardt, J.; Yang, P. D. *J. Phys. Chem. B* **2006**, *110*, 22652.
- (55) Park, K.; Zhang, Q. F.; Garcia, B. B.; Zhou, X. Y.; Jeong, Y. H.; Cao, G. Z. *Adv. Mater.* **2010**, in press.

Dyes and Ligands for Dye-sensitized Solar Cells

For a complete list of OPV dye materials, please visit aldrich.com/opvdyes

| Name | Structure | Purity | Spectroscopic Properties | Cat. No. |
|--|-----------|-----------------------------------|---|---|
| Di-tetrabutylammonium <i>cis</i> -bis(isothiocyanato)bis(2,2'-bipyridyl-4,4'-dicarboxylato)ruthenium(II), N-719 | | 95%, NMR, Dye content ≥90% (HPLC) | λ_{max} 534 nm, 313 nm, 393 nm | 703214-250MG |
| <i>cis</i> -Bis(isothiocyanato)(2,2'-bipyridyl-4,4'-dicarboxylato)(4,4'-di-nonyl-2'-bipyridyl)ruthenium(II), Z-907 | | 95%, NMR, Dye content ≥90% | λ_{max} 314 nm, 295 nm, 531 nm | 703168-250MG |
| <i>cis</i> -Bis(isothiocyanato)bis(2,2'-bipyridyl-4,4'-dicarboxylato)ruthenium(II), N-3 | | 95%, NMR | λ_{max} 312 nm, 534 nm, 395 nm | 703206-250MG |
| Benzo[e]pyrene | | 99% | - | B10102-25MG B10102-100MG |
| Coumarin 153 | | Dye content 98% | λ_{max} 422 nm, λ_{em} = 532 nm in ethanol | 546186-100MG |
| 1,3-Bis[4-(dimethylamino)phenyl]-2,4-dihydroxycyclobutenediylidium dihydroxide, bis(inner salt) | | Dye content 90% | λ_{max} 625 nm | 149063-1G |
| Coumarin 102 | | Dye content 99% | λ_{max} 390 nm, λ_{em} = 466 nm in ethanol | 546151-100MG |
| Coumarin 30 | | Dye content 99% | λ_{max} 413 nm, λ_{em} = 478 nm in ethanol | 546127-100MG |
| Coumarin 6 | | ≥99% | λ_{max} 443 nm, λ_{em} = 505 nm in ethanol | 546283-100MG |
| Pyrene | | 99% | λ_{em} = 375 nm in DMSO | 571245-1G |

| Name | Structure | Purity | Spectroscopic Properties | Cat. No. |
|--|---|--------|--------------------------|---|
| Quinoline |  | 98% | - | 241571-5G 241571-100G 241571-500G |
| 4,4'-Dinonyl-2,2'-dipyridyl, dNbpy |  | 97% | - | 482250-1G 482250-5G |
| 2,2'-Bipyridine-4,4'-dicarboxylic acid |  | 98% | - | 550566-1G |
| 2,2'-Bipyridine-3,3'-diol |  | 98% | - | 340081-50MG |

Nanopowders for Photovoltaic Applications

For a complete list of materials for energy generation and storage, please visit aldrich.com/renewable

| Name | Purity | Dimensions | Cat. No. |
|---|---------------------------|---|--|
| Titanium(IV) oxide, anatase, nanopowder | 99.7% trace metals basis | particle size <25 nm, spec. surface area 200-220 m ² /g | 637254-50G 637254-100G 637254-500G |
| Titanium(IV) oxide, rutile, nanopowder | 99.5% trace metals basis | particle size <100 nm, spec. surface area 130-190 m ² /g | 637262-25G 637262-100G 637262-500G |
| Titanium(IV) oxide, mixture of rutile and anatase, nanopowder | 99.5% trace metals basis | particle size <100 nm (BET) particle size <50 nm (XRD) | 634662-25G 634662-100G |
| Titanium(IV) oxide, nanopowder | ≥99.5% trace metals basis | particle size ~21 nm, spec. surface area 35-65 m ² /g (BET) | 718467-100G |
| Zinc oxide, nanopowder | - | particle size <100 nm, surface area 15-25 m ² /g | 544906-10G 544906-50G |
| Zinc oxide, nanopowder | >97% | particle size <50 nm (TEM), surface area >10.8 m ² /g | 677450-5G |

Nanoparticle Dispersions*

| Name | Purity | Dimensions | Concentration | Cat. No. |
|---|--------------------------|---|--|---------------------------|
| Iron oxide, dispersion, nanoparticles | - | avg. part. size <30 nm (APS) particle size <110 nm (DLS) | 20 wt. % in ethanol | 720712-100G |
| Iron oxide, dispersion, nanoparticles | - | avg. part. size <30 nm (APS) particle size <100 nm (DLS) | 20 wt. % in H ₂ O | 720704-100G |
| Titanium(IV) oxide, mixture of rutile and anatase, nanoparticles paste | 99.9% trace metals basis | particle size <250 nm (DLS) particle size ~21 nm (primary particle size of starting nanopowder), BET surf. area 50 m ² /g (BET surface area of starting nanopowder) | 53-57 wt. % in diethylene glycol monobutyl ether/ethylene glycol | 700355-25G |
| Titanium(IV) oxide, mixture of rutile and anatase, dispersion nanoparticles | 99.9% trace metals basis | particle size <150 nm (DLS) particle size ~21 nm (primary particle size of starting nanopowder) | 33-37 wt. % in H ₂ O | 700347-25G 700347-100G |
| Titanium(IV) oxide, mixture of rutile and anatase, dispersion nanoparticles | 99.9% trace metals basis | particle size <100 nm (DLS) particle size ~15 nm (primary particle size of starting nanopowder), BET surf. area 90 m ² /g (BET surface area of starting nanopowder) | 45-47 wt. % in xylene | 700339-100G |
| Zinc oxide, dispersion, nanoparticles | - | avg. part. size <35 nm (APS) particle size <100 nm (DLS) | 50 wt. % in H ₂ O | 721077-100G |
| Zinc oxide, dispersion, nanoparticles | - | avg. part. size <35 nm (APS) particle size <130 nm (DLS) | 40 wt. % in ethanol | 721085-100G |
| Zinc oxide, dispersion, nanoparticles | - | avg. part. size <35 nm (APS) particle size <110 nm (DLS) | 40 wt. % in butyl acetate | 721093-100G |
| Zinc oxide, dispersion, nanoparticles | - | avg. part. size <35 nm (APS) particle size <120 nm (DLS) | 40 wt. % in butyl glycol | 721107-100G |

*Products of Buhler, Inc.

Precursors for Atomic Layer Deposition

High-Tech Solutions for Your Research Needs

Nano-layers of metals, semiconducting and dielectric materials are crucial components of modern electronic devices, high-efficiency solar panels, memory systems, computer chips and a broad variety of high-performance tools.

The technique of choice for depositing nano-films on various surfaces is Atomic Layer Deposition (ALD), which uses consecutive chemical reactions on a material's surface to create nanostructures with predetermined thickness and chemical composition (**Figure 1**).

Aldrich Materials Science offers high-quality precursors for ALD safely packaged in steel cylinders suitable for use with a variety of deposition systems.

We continue to expand our portfolio of ALD precursors to include new materials. For an updated list of our deposition precursors, please visit aldrich.com/ald.

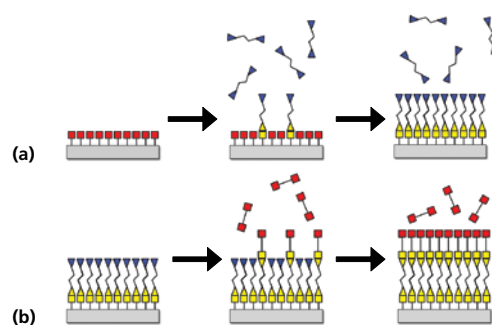


Figure 1. Schematic of the ALD method based on sequential, self-limiting surface reactions.



Precursors Packaged for Deposition Systems

| Atomic No. | Description | Molecular Formula | Form | Prod. No. |
|------------|--|--|--------|-----------|
| | Water packaged for use in deposition systems | H ₂ O | liquid | 697125 |
| 13 | Trimethylaluminum | (CH ₃) ₃ Al | liquid | 663301 |
| 14 | (3-Aminopropyl)triethoxysilane | H ₂ N(CH ₂) ₃ Si(OC ₂ H ₅) ₃ | liquid | 706493 |
| 14 | Silicon tetrachloride | SiCl ₄ | liquid | 688509 |
| 14 | Tris(<i>tert</i> -butoxy)silanol | ((CH ₃) ₃ CO) ₃ SiOH | solid | 697281 |
| 14 | Tris(<i>tert</i> -pentoxy)silanol | (CH ₃ CH ₂ C(CH ₃) ₂ O) ₃ SiOH | liquid | 697303 |
| 22 | Tetrakis(diethylamido)titanium(IV) | [(C ₂ H ₅) ₂ N] ₄ Ti | liquid | 725536 |
| 22 | Tetrakis(dimethylamido)titanium(IV) | [(CH ₃) ₂ N] ₄ Ti | liquid | 669008 |
| 22 | Titanium tetrachloride | TiCl ₄ | liquid | 697079 |
| 22 | Titanium(IV) isopropoxide | Ti[OCH(CH ₃) ₂] ₄ | liquid | 687502 |
| 30 | Diethylzinc | (C ₂ H ₅) ₂ Zn | liquid | 668729 |
| 39 | Tris[N,N-bis(trimethylsilyl)amide]yttrium | (((CH ₃) ₃ Si) ₂ N) ₃ Y | solid | 702021 |
| 40 | Bis(methyl-η5-cyclo-pentadienyl)methoxymethylzirconium | Zr(CH ₃ C ₅ H ₄) ₂ CH ₃ OCH ₃ | liquid | 725471 |

| Atomic No. | Description | Molecular Formula | Form | Prod. No. |
|------------|---|---|-------------------|-----------|
| 40 | Tetrakis(dimethylamido)zirconium(IV) | [(CH ₃) ₂ N] ₄ Zr | solid | 669016 |
| 40 | Tetrakis(ethylmethylamido)zirconium(IV) | C ₁₂ H ₂₃ N ₄ Zr | liquid | 725528 |
| 44 | Bis(ethylcyclopentadienyl)ruthenium(II) | C ₇ H ₉ RuC ₇ H ₉ | liquid | 679798 |
| 72 | Bis(methyl-η5-cyclopentadienyl)dimethylhafnium | Hf[(C ₅ H ₄ (CH ₃) ₂)(CH ₃) ₂] | solid | 725501 |
| 72 | Bis(methyl-η5-cyclopentadienyl)methoxymethylhafnium | HfCH ₃ (OCH ₃)[C ₅ H ₄ (CH ₃) ₂] | liquid | 725498 |
| 72 | Tetrakis(dimethylamido)hafnium(IV) | [(CH ₃) ₂ N] ₄ Hf | low-melting solid | 666610 |
| 72 | Tetrakis(ethylmethylamido)hafnium(IV) | [(CH ₃)(C ₂ H ₅)N] ₄ Hf | liquid | 725544 |
| 73 | Tris(diethylamido)(<i>tert</i> -butylimido)tantalum(V) | (CH ₃) ₃ CNTa(N(C ₂ H ₅) ₂) ₃ | liquid | 668990 |
| 74 | Bis(<i>tert</i> -butylimino)bis(dimethylamino)tungsten(VI) | ((CH ₃) ₃ CN) ₂ W(N(CH ₃) ₂) ₂ | liquid | 668885 |
| 78 | Trimethyl(methylcyclopentadienyl)platinum(IV) | C ₅ H ₄ CH ₃ Pt(CH ₃) ₃ | low-melting solid | 697540 |

For additional vapor deposition precursors prepacked in cylinders, please contact us by email at matsci@sial.com.

Nanomaterials for Energy Storage in Lithium-ion Battery Applications



Ganesh Venugopal¹, Andrew Hunt¹, and Faisal Alamgir²

¹nGimat Co., 5315 Peachtree Blvd., Atlanta, GA, USA

²Georgia Institute of Technology, Department of Materials Science and Engineering
771 Ferst Drive, N.W., Atlanta, GA 30332

Email: gvenugopal@ngimat.com, ahunt@ngimat.com, faisal@mse.gatech.edu

Introduction

Rechargeable Lithium-ion (Li-Ion) battery technology has come a long way since its introduction in the early 1990s. Over the last two decades, they have become the technology of choice for powering portable electronic devices such as cellular phones and laptop computers. Currently, Lithium-ion batteries are steadily replacing Nickel-Cadmium (NiCd) and Nickel-Metal Hydride (NiMH) battery technologies in portable power tools. In the future, Lithium-ion batteries are poised to power a new generation of hybrid electric vehicles (HEV), plug-in hybrids (PHEV) and electric vehicles (EV). Another emerging application for Lithium-ion technology is in battery electrical energy storage systems for smart grids that are powered by traditional energy sources like coal, as well as intermittent renewable energy sources like solar and wind.¹

The optimum combination of long run time (high energy density at the desired power) and long life (recharge characteristics) sets Lithium-ion battery technology apart from the competition. Needless to say, safety and cost expectations of the application also have to be satisfied. While all of these requirements are being met for portable electronics, the technology is just beginning to move up the optimization curve for emerging applications such as electric automotives, power tools and storage systems. For example, one factor that distinguishes the portable electronics and the electric vehicle application is power density. The latter requires much higher charge and discharge rates compared to the former. While higher power can be achieved to some extent by redesigning the way the battery cell is constructed, nanomaterials are also expected to play a key role in the achievement of high-power capability. Nanomaterial strategies are also being employed to provide better strain accommodation in high-capacity electrodes so that this storage capacity can be extracted reversibly with minimum compromise in cycle life. Alternatively, the stable cycle life and storage life characteristics of "zero-strain" electrode materials can be improved even further by utilizing nanosized versions of these electrodes, thereby providing a new generation of electrical energy storage options for smart grids and back-up power systems.

Overview of Lithium-ion Electrode Materials Chemistries

Conventional Lithium-ion battery materials typically start as 10-50 micron sized particles, which are then coated onto aluminum or copper current collectors along with conductivity enhancers and binders. The work-horse cathode chemistry for the last couple of decades has been Lithium Cobalt Oxide, LiCoO₂, (Aldrich Prod. No. 442704), a layered compound with a distorted rock-salt (α -NaFeO₂) structure.² Some alternative cathodes, like the three dimensional spinel Lithium Manganese Oxide,² LiMn₂O₄, (Aldrich Prod. No. 725129) have been commercialized only in niche applications, because of performance

limitations.² Carbon-based materials have been the preferred choice for anodes, with some version of graphite being utilized in a majority of the commercially available batteries.³ Battery developers choose electrode materials with the intent to optimize performance from the standpoints of energy, power, cycle life, cost and thermal stability. Until recently, much of this optimization has taken place with the portable electronic application in mind. More recently however, a significant effort is also being spent on new and emerging applications like power tools, electric vehicles and battery electrical energy storage systems. New chemistries have emerged for cathodes including a variety of mixed metal oxides, like LiMn_{1.5}Ni_{0.5}O₄ (spinel, Aldrich Prod. No. 725110), LiNi_{0.33}Mn_{0.33}Co_{0.34}O₂ (layered) and LiNiCoAlO₂ (layered) and metal phosphates, like LiFePO₄, LiCoPO₄ (Aldrich Prod. No. 725145) and LiMnPO₄, (olivine).^{2,4} For anodes, new materials include oxides such as Lithium Titanates (Li₄Ti₅O₁₂) & Tin Oxide (SnO₂, Aldrich Prod. No. 549657), elemental silicon (Si, Aldrich Prod. No. 267414) & tin (Sn, Aldrich Prod. No. 265640) and many carbon-based materials.^{3,5} In many of these new chemistries, having the materials in nanoparticle form or as a nanostructured particle or film is critical to achieving the desired performance dictated by the end application.⁵

Advantages of Nanomaterials for Lithium-ion Applications

From the battery application perspective, the incentive for implementing a nanomaterial electrode as a Lithium-ion storage material would be to derive significant improvement in energy, power, cycle life or some combination of the same. Nanoparticles or nanopowder electrode materials, i.e., ultrafine versions of the conventional micron-sized electrode powders, are the earliest implementation of nanomaterials science in the Lithium-ion battery application. Indeed, carbon-black, a nanomaterial that has been around for several decades, has been used in Lithium-ion batteries since its early days.⁷ While carbon-black is used in the electrode, it does not store electrical energy and merely acts as a "passive" conductivity enhancer to improve power capability. However, by designing the "active" energy storage component of the electrode as a nanoparticle, significant performance improvements can be realized for two reasons: 1) shorter diffusion lengths for the Lithium-ion travelling from the particle core to the surface where it transfers to the electrolyte and 2) higher electrode-electrolyte contact area arising from the inherently high surface areas characteristic of the particles.⁵

Reducing electrode particle size into the nanoscale regime is also believed to substantially reduce the mechanical stresses caused by volumetric expansion and contraction during charge and discharge. A recently developed model suggests that particles must have a size under a certain critical radius so that the strain produced by intercalation can be accommodated elastically, rather than by plastic deformation, allowing for the full recovery of the original, stable structure.⁸ Examples of nanomaterials either in nanopowder form or as nanostructured films with wire, rod, whisker or columnar morphologies are actively being pursued to maximize cycle life with minimum compromise in energy density.^{5,9}

Some processing advantages may also be realized while working with nanosized Li-ion storage electrode materials. For example, most Lithium-ion cathode materials are made from precursors containing lithium and other transition metals, which are combined and then heat treated under a variety of conditions to arrive at the desired oxide or phosphate composition. Heat treatment processes can be tedious and energy-intensive, particularly for large particle aggregates where the surface of the aggregate may experience a different thermal profile

compared to the bulk. Improper heat treatment leads to non-homogeneous composition in the material and hence deterioration in performance. While heat treating nanomaterials, it is easier to maintain a homogenous thermal profile throughout the material and thereby produce homogenous compositions without having to resort to energy-intensive processing methods.

Nanomaterials could also enable ultrathin and flexible electrode geometries, which may spawn a new generation of high-rate battery formats for low profile components such as sensors, RFID and flexible devices for consumer and medical applications. Dispersions and inks made using nanopowder electrodes could be used to fabricate low-cost printed batteries via roll-to-roll processing or to integrate thin-film batteries with other devices in printed electronic assemblies made via ink-jet processes.¹⁰

Classification and Production of Nanomaterials

The term nanomaterial is typically used to refer to materials that have at least one dimension of less than 100 nm.¹¹ In using the term, there is also an underlying implication that the material has some enhanced property or characteristic compared to larger particle size versions of the same composition. Nanomaterials are not a new class of materials, even though the recent attention that they have been garnering may suggest otherwise. Some of these materials, like volcano dust, have existed in nature forever. Other man-made materials, like carbon black and fumed titania (TiO₂), have been around for several decades. One way to classify nanomaterials is to categorize them according to the method by which they are produced, i.e., physical or chemical. The physical method can be further sub-divided into mechanical or phase-change methods. In the physical-mechanical method, particles in the nanometer size range are produced by milling or grinding larger particles of the target composition without any accompanying chemical change.¹² This method is commonly referred to as a “top-down” approach to making nanomaterials. In physical-phase change methods, the nanomaterial is created via a phase change process. Examples include direct precipitation, in which a material in solution is precipitated as a solid nanomaterial, and thermal, plasma or laser ablation processing in which vaporized material is condensed into solid nanoparticles. In using either of the physical processes, no chemical change is necessary to arrive at the target nanomaterial composition. Chemical methods include processes where the nanomaterial is synthesized from an initial material that is chemically different from the target composition. The target composition is arrived at via chemical synthesis of a solid that is formed directly in the nanoscale. Examples include flame pyrolysis, spray pyrolysis and wet-chemical methods such as sol-gel and solvo-thermal synthesis.¹² The chemical method and the physical-phase change method are both examples of the “bottom-up” approach to making nanomaterials.

An example of a chemical process for making nanomaterials is NanoSpray Combustion, invented by one of the authors, where nanoparticles or nanopowders are produced via combustion chemical vapor condensation (nCCVC).¹³ In this process, nanoparticles are produced by the combustion of a solution nanospray that consists of precursors that contain the elements that eventually make up the nanoparticle. A schematic of this process is shown in **Figure 1**. nGimat’s proprietary Nanomiser® device is critical to generating the nanospray from which vapor species are formed in the flame. Condensation of particles can take place either in dry form nanopowders or into a liquid medium to form dispersions. By tailoring precursor formulations and process parameters, nCCVC can be also be used to produce nanomaterials with dopants and surface carbon-coatings to improve performance in the end application.

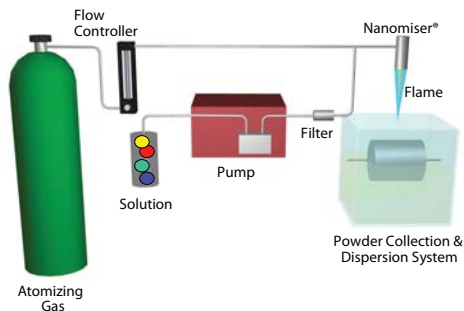


Figure 1. Schematic of the NanoSpray combustion chemical vapor condensation (nCCVC) process for making nanopowders.

While nanoparticles or nanopowders are by definition less than 100 nm in size, other nanomaterials may exhibit structural features that are <100 nm, while existing as larger aggregates like secondary particles or films. For example, lithographic patterning, chemical vapor deposition and physical vapor deposition are all capable of producing nano-structured films with complex structures and are often referred to as form-in-place techniques.¹² A variation of nCCVC, called combustion chemical vapor deposition (nCCVD) can also be classified in this category.¹⁴ This process has been used to make nanostructured thin film coatings with super-hydrophobic, antimicrobial, oxygen-barrier and moisture-barrier characteristics. The nCCVD process has also been used to deposit battery electrode materials.⁵ In the following sections, we will focus on the application of nanoparticles or nanopowders in Lithium-ion batteries.

Lithium-ion Battery Application of Nanopowders Made by nCCVC

Using the nCCVC process described above, it is possible to produce a variety of Lithium-ion electrode material compositions that are being pursued by the battery community. The nCCVC process is very well-suited for making metal oxides and metal phosphate materials. **Figure 2** shows the transmission electron micrographs (TEM) of two representative compounds, LiCoPO₄ and LiMn_{1.5}Ni_{0.5}O₄. The two materials show different particle morphologies; the former shows spherical features, while the latter is composed of faceted particles. In both cases, the average particle size is well under 100 nm. The higher magnification picture of the LiMn_{1.5}Ni_{0.5}O₄ nanoparticle reveals the crystalline structure of the nanoparticle.

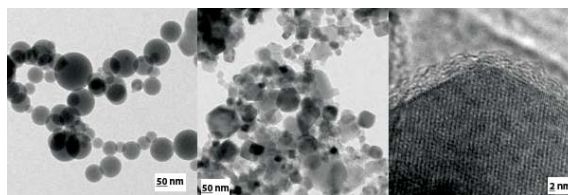


Figure 2. Transmission electron micrographs showing nanoparticles of Lithium Cobalt Phosphate, LiCoPO₄ (left), Lithium Manganese Nickel Oxide, LiMn_{1.5}Ni_{0.5}O₄ (center), and Lithium Manganese Nickel Oxide, LiMn_{1.5}Ni_{0.5}O₄ (right) at higher magnification.

Both LiMn_{1.5}Ni_{0.5}O₄ and LiCoPO₄ are candidates for high-voltage Li-ion cathodes for a new generation of Lithium-ion batteries.² For example, LiMn_{1.5}Ni_{0.5}O₄ can be charged up to the 4.8–5.0V range compared to 4.2–4.3V charge voltage for LiCoO₂ and LiMn₂O₄.¹⁵ The higher voltages, combined with the higher theoretical capacity of around 155 mAh/g for LiMn_{1.5}Ni_{0.5}O₄ enable a 25% improvement in energy density compared to conventional Lithium-ion cathodes. Other examples of cathode nanomaterials synthesized by nCCVC include LiCoPO₄, spinel LiMn₂O₄ and orthorhombic LiMnO₂ (Aldrich Prod. No. 725137).

The X-ray diffraction (XRD) patterns of the above-mentioned cathode material and representative anode materials made by nCCVC are shown in **Figure 3**. All of the patterns match well with reference patterns published by in the literature.¹⁶ Candidate anode nanomaterials made by nCCVC include SnO₂ and Li₄Ti₅O₁₂ (Aldrich Prod. No. 702277). These materials are targeted for different ends of the applications spectrum. SnO₂ is a candidate for a high energy density anode with theoretical capacities reaching upward of 750 mAh/g and a voltage of <1V vs. lithium metal, compared to 370 mAh/g and <0.5V for the conventional graphite anodes of today.^{5,6} Lower voltages are typically desired for anodes so as to maximize the voltage and energy when coupled with a corresponding higher-voltage cathode. Li₄Ti₅O₁₂, on the other hand, has a capacity of around 160 mAh/g at nominal voltages of around 1.5V.¹⁷ Although it has a lower energy density, its zero-strain spinel structure can accept many charge-discharge cycles with a minimum loss in capacity. Furthermore, when used in nanopowder form, Li₄Ti₅O₁₂ is also known to provide high charge and discharge rate capabilities, as shown below.

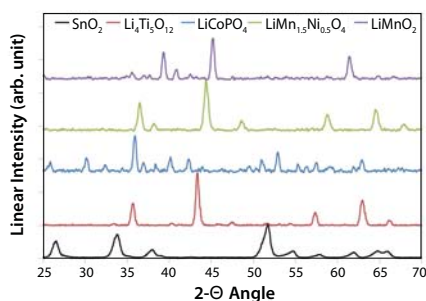


Figure 3. X-ray diffraction patterns for Tin Oxide (SnO₂), Lithium Titanate (Li₄Ti₅O₁₂), Lithium Cobalt Phosphate (LiCoPO₄), Lithium Manganese Nickel Oxide (LiMn_{1.5}Ni_{0.5}O₄) and Lithium Manganese Oxide (LiMnO₂) nanopowders made with the nCCVC process.¹⁶

Representative discharge voltage profiles for three of the nanopowder electrodes synthesized by nCCVC are shown in **Figure 4** below. This data was acquired with small prototype cells which used Lithium-metal as the counter-electrode. The two curves on the upper end of the chart represent 0.1C-rate profiles for cathode materials LiCoPO₄ and LiMn_{1.5}Ni_{0.5}O₄ and as anticipated both materials demonstrate high-voltage plateaus in the 4.7–4.8V range. The lower curve represents the C-rate profile for Li₄Ti₅O₁₂ and this material demonstrates a flat discharge curve with a plateau at around 1.5V.

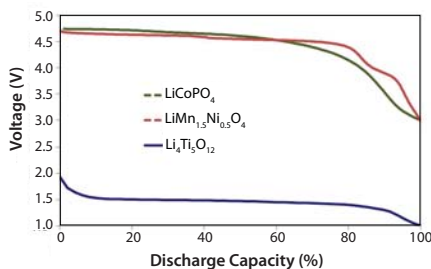


Figure 4. Discharge voltage profiles for three representative Lithium-ion storage nanopowders made by nCCVC and assembled in prototype half-cells with a Lithium-metal anode: Lithium Titanate, Li₄Ti₅O₁₂ (blue line, bottom) and Lithium Cobalt Phosphate, LiCoPO₄ and Lithium Manganese Nickel Oxide, LiMn_{1.5}Ni_{0.5}O₄ (red and green lines, top).

The high-rate discharge capability of the nanomaterials has also been demonstrated in prototype cells for the Li₄Ti₅O₁₂ materials. As shown in **Figure 5**, Li₄Ti₅O₁₂ can be discharged at 5C and 10C continuous rates and can retain up to 80% and 60% of the C-rate capacities respectively. In comparison, conventional cathode materials like LiCoO₂ are typically not recommended for use over 3C-rates. Typical discharge capacities for the Li₄Ti₅O₁₂ nanomaterials at C-rate have been around 145 mAh/g. The Li₄Ti₅O₁₂ materials have also been cycled for >200 cycles at C-rate. This is highly encouraging performance for the nanomaterial, considering that the test-vehicle is only a lab-assembled prototype cell format. The performance of the material can be expected to improve significantly when assembled using processes that are closer to commercial cell manufacturing methods.

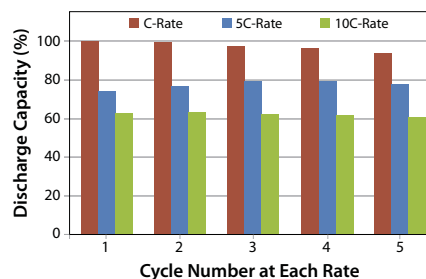


Figure 5. Comparison of the relative capacities achieved at high discharge rates (5C and 10C) vs. capacity achieved at 1C discharge rate over 16 cycles for a Li₄Ti₅O₁₂-Lithium-metal half-cell in prototype format.

Under the right conditions, the nCCVC process will allow the formation of surface coatings on the electrode particles. Direct coating of the electrode particles with carbon provides higher electronic conductivity to enhance rate capability of the battery. Surface-coated carbon may also eliminate the need for additional conductivity enhancers like carbon-black in the coated electrodes, providing opportunities to increase the energy density of the cell. By tailoring the precursor system and the nCCVC processing conditions, it is possible to make carbon-coated Li₄Ti₅O₁₂ nanopowders with a single step process.¹² In conventional methods used to process Lithium-ion electrode materials, a separate down-stream processing step is required for making carbon-coated materials.¹⁸

Carbon nanotubes (CNT) are also considered to be promising candidates for a high performance Lithium-ion anodes due to their high surface area and also their outstanding electrical and mechanical properties.¹⁹ However, the experimental results show only a 20-25% increase for reversible capacity compared to graphite electrode because of weak lithium adsorption to CNTs.²⁰ To improve Li adsorption, researchers have used either chemical/plasma etching for making defects or fullerene (C₆₀) encapsulation of single-walled carbon nanotubes for the creation of fullerene "peapods."^{21,22} In some cases, materials with a maximum capacity of ~1,000 mAh/g, corresponding to Li_{2.7}C₆, are produced. However, these methods require complex and high-temperature processing, often leading to deterioration in their performance.

The Future for Lithium-ion Energy Storage Materials

Emerging applications have steered Lithium-ion materials R&D in a new direction, which includes development of nanomaterial electrodes. Early versions of these nanomaterials are already beginning to appear in limited quantities in the marketplace, primarily in portable power tool applications. Within the next few years, Lithium-ion nanomaterials can also be expected to appear in automotive applications like PHEV and also in battery electrical energy storage systems. Existing applications like portable electronics, where Lithium-ion technology is fully entrenched, could also benefit from the implementation of nanomaterial electrodes that provide high-capacity at the desired power-levels without compromising cycle life.

While adapting to the electrical performance requirements of the emerging applications, the materials and the processes used to make them have to be aware of the cost-sensitivity in the marketplace. Reduction in raw materials cost and consolidation of multiple steps in the process will be critical to any commercialization effort. Since Lithium-ion electrodes pack more energy and are in the proximity of non-aqueous electrolytes, they will also incur higher packaging costs at the cell-level and at the battery pack-level, compared to Nickel-Metal Hydride systems. Thermal cut-off devices in the cells and safety circuits and thermal management systems in the packs will ensure that the battery is well within its safe operating limit. In the long run, the performance premium offered by Lithium-ion batteries will more than off-set the added costs, particularly with economies of scale.

Acknowledgments

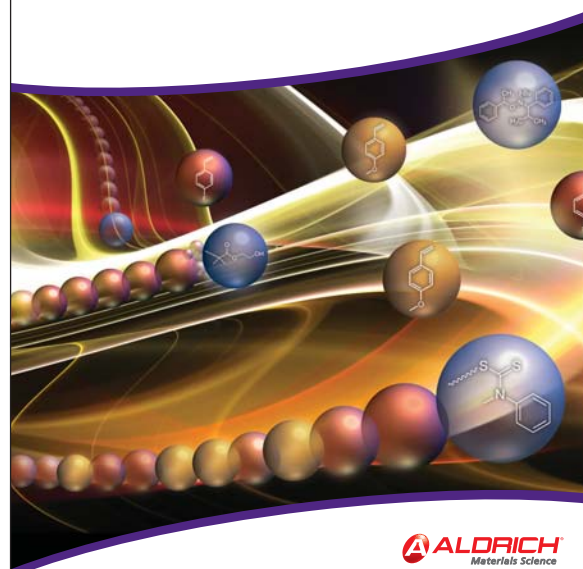
The authors would like to thank other members of the nGimat team for their contribution to the work described in this article. In particular, we would like to acknowledge Michael Sapp, Nina Vylkov, Chris Rockett, Yongdong Jiang and David Krauss. Transmission electron microscopy of our materials was performed by Dr. Yong Ding at the Georgia Institute of Technology. We would also like to acknowledge the financial support provided by U.S. Department of Energy (DOE) through research grants for the development and scale-up of Lithium-ion battery nanomaterials.

References

- (1) Scrosati, B.; Garche, J. *J. Power Sources*, **2010**, *195*, 2419.
- (2) Fergus, J. *J. Power Sources*, **2010**, *195*, 939.
- (3) Shukla, A. K.; Prem Kumar, T. *Curr. Sci.*, **2008**, *94*, 314.
- (4) Thackeray, M. J. *Chem. Eng. Japan*, **2007**, *40*, 1150.
- (5) Zhang, Y.; Liu, Y.; Liu, M. *Chem. Mater.*, **2006**, *18*, 4643.
- (6) Manthiram, A.; Murugan, A.V.; Sarkar, A.; Muraliganth, T. *Energy Environ. Sci.*, **2008**, *1*, 62.
- (7) Chen, Y.-H.; Wang, C.-W.; Liu, G.; Song, X.-Y.; Battaglia, V. S.; Sastry, A. M. *J. Electrochem. Soc.*, **2007**, *154*, A978.
- (8) Huggins, R. A.; Nix, W. D. *Ionics*, **2000**, *6*, 57.
- (9) Teki, R.; Datta, M. K.; Krishnan, R.; Parker, T. C.; Lu, T.-M.; Kumta, P. N.; and Koratkar, N. *Small* **2009**, *5*, 2236.
- (10) Zhao, Y.; Liu, G.; Liu, L.; Jiang, Z. *J. Solid State Electrochem.*, **2009**, *13*, 705.
- (11) ASTM Standards Document E2456, **2006**
- (12) Hunt, A.; Jiang, Y.; Zhang, Z.; Venugopal, G. Chapter 5, *Nano-Bio-Electronic, Photonic and MEMS Packaging*, (Edited by Wong, C. P., Moon, K.-Y., Li, Y.) Springer, **2010**
- (13) Oljaca, M.; Xing, Y.; Lovelace, S.; Shanmugham, S.; Hunt, A. *J. Mater. Sci. Lett.*, **2002**, *21*, 621.
- (14) Hunt, A. T.; Carter, B.; Cochran, J. *Appl. Phys. Lett.*, **1993**, *63*, 266.
- (15) Liu, D.; Han, J.; Goodenough, J. B. *J. Power Sources*, **2010**, *195*, 2918.
- (16) ICDD JCPDS Reference numbers: Tin Oxide: 21-1250, Lithium Titanate: 26-1198, Lithium Cobalt Phosphate: 32-0552, Lithium Manganese Nickel Oxide: 32-0581 & 80-2162, Lithium Manganese Oxide: 35-0749
- (17) Belharouak, I.; Sun, Y.-K.; Lu, W.; Amine, K. I. *J. Electrochem. Soc.*, **2007**, *154*, A1083.

- (18) Amine, K.; Belharouak, I.; Liu, J. **2007**, *US Patent* 2007/014845A1
- (19) Hong, S.; Myung, S. *Nanotech.*, **2007**, *2*, 207.
- (20) Zhou, Z.; Zhao, J.; Gao, X.; Chen, Z.; Yan, J.; Schleyer, P. R.; Morinaga, M. *Chem. Mater.*, **2005**, *17*, 992.
- (21) Shimoda, H.; Gao, B.; Tang, X. P.; Kleinhammes, A.; Fleming, L.; Wu, Y.; Zhou, O. *Phys. Rev. Lett.*, **2002**, *88*, 015502.
- (22) Kawasaki, S.; Iwai, Y.; Hirose, M. *Mater. Res. Bull.*, **2009**, *44*, 415.

We Focus on Materials So You Can Focus on Results



Material Matters™

A Quarterly Periodical from Aldrich
Materials Science

- Hot Topics in high-tech materials research
- Theme-based technical reviews by leading experts
- Application-focused selections of products and services
- Product application notes



Have you seen these recent issues? If not, get your complimentary subscription today: aldrich.com/mm

sigma-aldrich.com

SIGMA-ALDRICH®
Materials Science

Electrode Materials for Lithium-ion Batteries

For a complete list of materials for energy generation and storage, please visit aldrich.com/renewable

| Name | Linear Formula | Description | Cat. No. |
|---------------------------------|--|--------------------------|--------------------------|
| Lithium | Li | 99%, metals basis | 444456-10G 444456-50G |
| Lithium cobalt(III) oxide | LiCoO ₂ | 99.8% trace metals basis | 442704-100G-A |
| Lithium iron(III) oxide | LiFeO ₂ | 95%, particle size <1 μm | 442712-100G-A |
| Lithium manganese(III,IV) oxide | LiMn ₂ O ₄ | particle size <5 μm | 482277-25G |
| Lithium molybdate | Li ₂ MoO ₄ | 99.9% trace metals basis | 400904-250G |
| Lithium cobalt phosphate | LiCoPO ₄ | particle size <0.5 μm | 725145-25G |
| Lithium manganese nickel oxide | Li ₂ Mn ₃ NiO ₈ | particle size <0.5 μm | 725110-25G |
| Lithium manganese dioxide | LiMnO ₂ | particle size <1 μm | 725137-25G |
| Lithium manganese oxide | LiMn ₂ O ₄ | particle size <0.5 μm | 725129-25G |

Nanopowders for Energy Applications

For a complete list of available nanoparticles and nanopowders, please visit aldrich.com/nanomaterials

| Name | Linear Formula | Description | Form | Cat. No. |
|---------------------------------------|---|--|-----------------------------|------------------------------|
| Aluminum cerium oxide | AlCeO ₃ | 99% trace metals basis, particle size <50 nm (BET) | nanopowder | 637866-10G 637866-50G |
| Barium ferrite | BaFe ₁₂ O ₁₉ | >97% trace metals basis, particle size <100 nm (BET) | nanopowder | 637602-25G |
| Barium strontium titanium oxide | (BaTiO ₃)(SrTiO ₃) | >99 wt. % trace metals basis (Ba, Sr, and Ti), particle size <100 nm | nanopowder | 633828-25G 633828-100G |
| Calcium oxide | CaO | 98%, particle size <160 nm (BET) | nanopowder | 634182-25G 634182-100G |
| Calcium phosphate, amorphous | Ca ₃ O ₇ P ₂ · H ₂ O | particle size <150 nm (BET) | nanopowder | 693871-5G |
| Cerium(IV) oxide | CeO ₂ | particle size <25 nm (BET) | nanopowder | 544841-5G 544841-25G |
| Cerium(IV) oxide, dispersion | CeO ₂ | particle size <25 nm | dispersion nanoparticles | 643009-100ML 643009-250ML |
| Cerium(IV)-zirconium(IV) oxide | (CeO ₂)(ZrO ₂) | 99.0% trace metals basis, particle size <50 nm (BET) | nanopowder | 634174-25G 634174-100G |
| Copper iron oxide | CuFe ₂ O ₄ | 98.5% trace metals basis, particle size <100 nm (BET) | nanopowder | 641723-10G 641723-50G |
| Copper zinc iron oxide | CuZnFe ₄ O ₄ | 98.5% trace metals basis, particle size <100 nm (BET) | nanopowder | 641650-10G 641650-50G |
| Hydroxyapatite | [Ca ₅ (OH)(PO ₄) ₃] _x | ≥97%, particle size <200 nm (BET) | nanopowder | 677418-5G 677418-10G |
| Hydroxyapatite, 5 wt% silica as doped | [Ca ₅ (OH)(PO ₄) ₃] _x | particle size <200 nm (BET) | nanopowder | 693863-5G |
| Hydroxyapatite | [Ca ₅ (OH)(PO ₄) ₃] _x | particle size <200 nm (BET) | dispersion nanoparticles | 702153-25ML |
| Iron-nickel alloy | Fe/Ni (0.55:0.45) | ≥97%, particle size <100 nm (BET) | nanopowder | 677426-5G |
| Lithium titanate, spinel | Li ₄ Ti ₅ O ₁₂ | >99%, particle size <100 nm (BET) particle size <100 nm (TEM) | nanopowder | 702277-25G |
| Magnesium aluminate, spinel | MgO·Al ₂ O ₃ | particle size <50 nm (BET) | nanopowder | 677396-5G |
| Magnesium oxide | MgO | particle size <50 nm (BET) | nanopowder | 549649-5G 549649-25G |
| Nickel cobalt oxide | NiO CoO | 99% trace metals basis, particle size <150 nm (BET) | nanopowder | 634360-25G 634360-100G |
| Nickel zinc iron oxide | NiZnFe ₄ O ₄ | ≥99% trace metals basis, particle size <100 nm (BET) | nanopowder | 641669-10G 641669-50G |
| Palladium | Pd | 99.9%, particle size <25 nm (TEM) | nanopowder | 686468-500MG |
| Platinum | Pt | ≥99.9%, particle size <50 nm (TEM) | nanopowder | 685453-250MG |
| Samarium strontium cobalt oxide | SmSrCO ₄ O _x | 99.9%, particle size <50 nm (BET) | nanopowder | 677442-5G |
| Silicon dioxide, alumina doped | (SiO ₂) _x (Al ₂ O ₃) _y | 99.99% trace metals basis, particle size <50 nm | dispersion nanoparticles | 701491-25ML 701491-100ML |
| Silver-copper alloy | CuAg ₂₅ | particle size <100 nm | nanopowder | 576824-5G |
| Silver-tin alloy | AgSn ₂₅ | 3.5% Ag basis ≥97%, particle size <150 nm | nanopowder | 677434-5G |



| Name | Linear Formula | Description | Form | Cat. No. |
|---------------------------------------|---|--|-----------------------------|------------------------------|
| Tin(IV) oxide | SnO ₂ | particle size <100 nm (BET) | nanopowder | 549657-5G 549657-25G |
| Titanium(IV) oxide | TiO ₂ | ≥97%, particle size <100 nm (BET) | nanopowder | 677469-5G |
| Titanium silicon oxide | (SiO ₂)(TiO ₂) | 99.8% trace metals basis, particle size <50 nm (BET) | nanopowder | 641731-10G 641731-50G |
| Tricalcium phosphate hydrate | Ca ₃ (PO ₄) ₂ · xH ₂ O | particle size <100 nm (TEM) particle size <200 nm (BET) | nanopowder | 693898-5G |
| Yttrium iron oxide | Y ₃ Fe ₅ O ₁₂ | 99.9% trace metals basis, particle size <100 nm (BET) | nanopowder | 634417-10G |
| Zinc iron oxide | ZnFe ₂ O ₄ | >99% trace metals basis, particle size <100 nm (BET) | nanopowder | 633844-10G 633844-50G |
| Zinc oxide | ZnO | >97%, particle size <50 nm (TEM) | nanopowder | 677450-5G |
| Zirconium(IV) oxide, dispersion | ZrO ₂ | particle size <100 nm (BET) | dispersion nanoparticles | 643122-100ML 643122-500ML |
| Zirconium(IV) oxide, dispersion | ZrO ₂ | particle size <100 nm (BET) | dispersion nanoparticles | 643025-100ML |
| Zirconium(IV) oxide-yttria stabilized | ZrO ₂ | particle size <100 nm (BET) | nanopowder | 544779-25G |
| Zirconium(IV) silicate | ZrSiO ₄ | 98.5% trace metals basis, particle size <100 nm (BET) | nanopowder | 634395-25G 634395-100G |

Carbon Nanomaterials

For a complete list of carbon nanotubes, functionalized carbon nanotubes, and carbon nanofibers, please visit aldrich.com/carbonnanomaterials

Carbon Nanotubes

| Name | Purity | Size | Production Method | Cat. No. |
|---|--|--|--|---|
| Carbon nanotube*, single-walled, CG-100 | ≥70% (carbon as SWCNT) | diameter 0.7-1.3 nm, L 450-2300 nm (mode: 800 nm; AFM) | Produced by CoMoCAT® catalytic CVD process | 704113-250MG 704113-1G |
| Carbon nanotube*, single-walled, CG-200 | >90% (carbon as SWCNT) | diameter 0.7-1.4 nm | Produced by CoMoCAT® catalytic CVD process. | 724777-250MG 724777-1G |
| Carbon nanotube*, single-walled, SG-65 | ≥77% (carbon as SWCNT) Chirality distribution: >50% (6,5) | diameter 0.7-0.9 nm, L 450-2000 nm (mode: 900 nm; AFM) | Produced by CoMoCAT® catalytic CVD process. | 704148-250MG 704148-1G |
| Carbon nanotube*, single-walled, SG-76 | ≥77% (carbon as SWCNT) Chirality distribution: >50% (7,6) | diameter 0.7-1.1 nm, L 300-2300 nm (mode: 800 nm; AFM) | Produced by CoMoCAT® catalytic CVD process. | 704121-250MG 704121-1G |
| Carbon nanotube, single-walled | 50-70% carbon basis | diam. × L 1.2-1.5 nm × 2-5 μm (bundle dimensions) | Produced by Arc method | 519308-250MG 519308-1G |
| Carbon nanotube, single-walled | 40-60 wt. % carbon basis | diam. × L 2-10 nm × 1-5 μm (bundle dimensions) 1.3-1.5 nm (individual SWNT diameter) | Produced by Arc method | 698695-1G 698695-5G |
| Carbon nanotube, double-walled | 50-80% carbon basis | O.D. × I.D. × L 5 nm × 1.3-2.0 nm × 50 μm | Produced by CVD method | 637351-250MG 637351-1G |
| Carbon nanotube, multi-walled | >7.5% MWCNT basis | O.D. × L 7-15 nm × 0.5-10 μm | Produced by Arc method | 412988-100MG 412988-2G 412988-10G |
| Carbon nanotube, multi-walled | 25-35% MWCNT basis | avg. part. size ~270 mesh avg. part. size <53 μm, I.D. × L 2-15 nm × 1-10 μm | Produced by Arc method | 406074-500MG 406074-1G 406074-5G |
| Carbon nanotube, multi-walled | >90% carbon basis | diam. × L 110-170 nm × 5-9 μm | Produced by CVD method | 659258-2G 659258-10G |
| Carbon nanotube**, multi-walled | >90% carbon basis | O.D. × I.D. × L 10-15 nm × 2-6 nm × 0.1-10 μm | Produced by Catalytic Chemical Vapor Deposition (CCVD) | 677248-5G 677248-25G |
| Carbon nanotube, multi-walled | >95% carbon basis | O.D. × I.D. × L 7-15 nm × 3-6 nm × 0.5-200 μm | Produced by CVD method. | 694185-1G 694185-5G |
| Carbon nanotube, multi-walled | >99% carbon basis | O.D. × L 6-13 nm × 2.5-20 μm 10 μm (average length, TEM) 12 nm (average diameter, HRTEM) | CVD followed by HCl demineralization | 698849-1G |
| Carbon nanotube*, multi-walled, SMW 100 | >95% carbon basis | O.D. × L 6-9 nm × >1 μm | Produced by CoMoCAT® catalytic CVD process. | 724769-25G 724769-100G |

*Product of SouthWest NanoTechnologies, Inc. (SWeNT)

**Product of Arkema, Inc.

Functionalized Carbon Nanotubes

| Name | Purity | Size | Labeling | Solubility | Cat. No. |
|---|---------------------|---|--|---|---------------------------|
| Carbon nanotube, single-walled, amide functionalized | 80-90% carbon basis | diam. × L 4-6 nm × 0.7-1.0 μm (bundle dimensions) | extent of labeling per 4-8 atom % (amide groups) | DMF 0.5-1.0 mg/mL (with sonication) acetone 0.5-1.0 mg/mL (with sonication) alcohols 0.5-1.0 mg/mL (with sonication) | 685380-100MG |
| Carbon nanotube, single-walled, carboxylic acid functionalized | >90% carbon basis | diam. × L 4-5 nm × 0.5-1.5 μm (bundle dimensions) | extent of labeling atom% carboxylic acid 1.5-3.0 | H ₂ O 0.1 mg/mL DMF 1.0 mg/mL | 652490-250MG 652490-1G |
| Carbon nanotube, single-walled, octadecylamine functionalized | 80-90% carbon basis | diam. × L 2-10 nm × 0.5-2 μm (bundle dimensions) | extent of labeling 30-40 wt. % (ODA) | THF 1 mg/mL carbon disulfide 1 mg/mL methylene chloride soluble toluene soluble chloroform soluble benzene soluble | 652482-100MG |
| Carbon nanotube, single-walled, poly(ethylene glycol) functionalized | >80% carbon basis | diam. × L 4-5 nm × 0.5-0.6 μm (bundle dimensions) | PEG:SWNT 20:80 (wt. ratio) | H ₂ O 5 mg/mL | 652474-100MG |
| Carbon nanotube, single-walled, polyaminobenzene sulfonic acid functionalized | 75-85% carbon basis | diam. × L 1.1 nm × 0.5-1.0 μm (bundle dimensions) | extent of labeling 65% (PABS, typical) | DMF 0.1 mg/mL ethanol 0.05 mg/mL H ₂ O 5.0 mg/mL (As determined by near-IR absorbance spectroscopy.) | 639230-100MG |

Carbon Nanofibers

| Name | Purity | Size | Production Method | Cat. No. |
|--|--|---|--|---------------------------------------|
| Graphite, nanofibers | carbon content >95% (trace metals analysis) | O.D. × I.D. × L 80-200 nm × 0.5-10 nm × 0.5-20 μm | - | 636398-2G 636398-10G 636398-50G |
| Graphite, platelet nanofibers | 99%, carbon content >99% (trace metals analysis) | W × L 50-250 nm × 0.5-5 μm | Catalytic CVD followed by HCl demineralization | 698830-1G |
| Carbon nanofibers, iron free graphitized* | ≥99.9% | W × L 50-150 nm × 20-200 μm | Vapor-grown carbon fiber | 719781-25G |
| Carbon nanofibers, graphitized* | ≥98% | W × L 50-150 nm × 20-200 μm | Vapor-grown carbon fiber | 719803-25G |
| Carbon nanofibers, pyrolytically stripped* | ≥98% | W × L 50-150 nm × 20-200 μm | Vapor-grown carbon fiber | 719811-25G |

*Product of Pyrograf Products, Inc.

Mesoporous Carbon Nanomaterials

For a complete list of mesoporous materials, please visit aldrich.com/mesoporous

| Name | Particle Size | Pore Size | Surface Area | Cat. No. |
|--|-------------------------------------|--|---|-------------------------|
| Carbon, mesoporous | particle size distribution 45 μm ±5 | average pore diameter 100 Å ±10 Å (typical) pore volume 0.5 cm ³ /g (typical) | spec. surface area 150-250 m ² /g | 699640-5G 699640-25G |
| Carbon, mesoporous, nanopowder | particle size <500 nm (DLS) | average pore diameter 64 Å (typical) total pore volume 0.342 cm ³ /g (typical) | spec. surface area 150-250 m ² /g | 699632-5G 699632-25G |
| Carbon, mesoporous, graphitized, nanopowder | particle size <500 nm (DLS) | average pore diameter 137 Å (typical) pore volume 0.25 cm ³ /g (typical) | spec. surface area 50-100 m ² /g | 699624-5G 699624-25G |
| Carbon, mesoporous, hydrophobic pore surface, Starbon® 800 | - | mesoporosity 0.4-0.7 cm ³ /g microporosity 0-0.2 cm ³ /g | spec. surface area 150-500 m ² /g (BET) | 702102-5G |
| Carbon, mesoporous, hydrophilic pore surface, Starbon® 300 | - | mesoporosity >0.4 cm ³ /g | mesopore surface area ≥130 m ² /g spec. surface area >300 m ² /g (BET) | 702110-5G |

Aldrich MOF Constructor

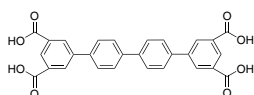
An Easy Way to Design your Own MOF

Metal-Organic Frameworks (MOFs) are porous coordination networks with record-setting surface areas. MOFs are built from metal ion clusters connected by organic linker molecules or struts. They are designed for specific applications requiring high surface area materials.

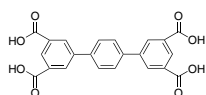
Aldrich Materials Science is uniquely positioned to assist you in constructing your own MOF. Please review our *current offering* of organic linkers, high-purity metal salts, and solvents, or request *custom-designed materials* to meet your research needs.

Organic Linker Molecules for Metal-Organic Frameworks

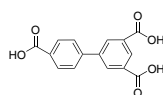
For a complete list of organic linker molecules for MOFs, please visit aldrich.com/moflinkers



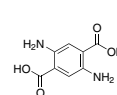
716499



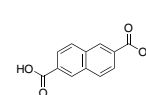
716502



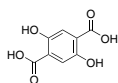
714747



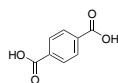
717312



523763



382132



185361



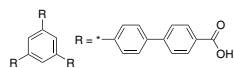
482749



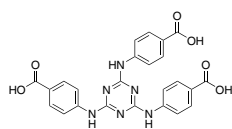
1202



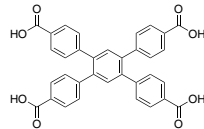
M50850



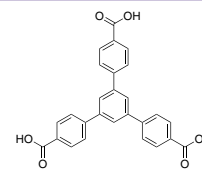
706884



719250



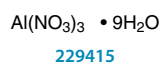
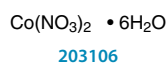
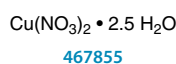
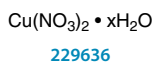
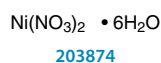
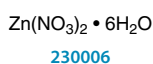
715298



686859

High-Purity Metal Salts for Synthesis of Metal-Organic Frameworks

For a complete list of metal salts and other related materials, please visit aldrich.com/ceramics



Selected Solvents for Synthesis of Metal-Organic Frameworks

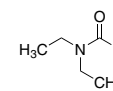
For a complete list of solvents offered by Sigma-Aldrich®, please visit aldrich.com/solvents



227056



437573



186317

Contact us at (800) 231-8327 to discuss materials for your own MOF. For more information, visit aldrich.com/renewable.

Perovskite-phase Metal Oxide Nanostructures: Synthesis, Properties, and Applications



Yuanbing Mao¹, Hongjun Zhou¹, and Stanislaus S. Wong^{1,2,*}

¹Department of Chemistry, State University of New York at Stony Brook, Stony Brook, NY 11794-3400

*Email: sswong@notes.cc.sunysb.edu

²Condensed Matter Physics and Materials Sciences Department, Brookhaven National Laboratory, Upton, NY 11973

*Email: sswong@bnl.gov

Properties of Perovskite Systems

Perovskite-phase metal oxides exhibit a variety of interesting physical properties which include ferroelectric, dielectric, pyroelectric, and piezoelectric behavior.¹⁻⁴ Specifically, linear dielectric materials exhibit linear polarization behavior as a function of applied field. Ferroelectric ceramics are dielectrics with a permanent electric dipole, which can be oriented upon the application of an electric field. Pyroelectric materials yield a spontaneous polarization, but the direction of such polarization cannot be reversed upon application of an electric field. Piezoelectrics either exhibit an electrical charge when mechanically stressed or undergo mechanical deformation upon the application of an electric field. In general, these various properties arise from the crystal symmetry adopted by these materials.^{5,6}

Of these various classes of structures, ferroelectric materials are both pyroelectric and piezoelectric and are generating a great deal of current interest because their electric dipoles can be reoriented by the application of an electric field. However, all of these materials lose their inherent polar properties above their Curie temperature (T_C) transforming into a nonpolar state known as the paraelectric phase. For example, barium titanate (BaTiO_3 , **Aldrich Prod. No. 467634**) alters from a tetragonal ferroelectric phase to a paraelectric cubic phase at a Curie temperature of 120 °C. The properties of ferroelectric materials change significantly and show a maximum as the temperature approaches T_C . Specifically, in the case of BaTiO_3 ,⁷ the dielectric constant increases from 1,000 to a value of ~10,000 in the 10 K interval below its T_C , while above this temperature, there is a gradual decrease in the dielectric constant. Hence, the main applications of BaTiO_3 are based around this phase transition, especially with respect to its potential as a dielectric. The temperatures at which these phase transitions occur can also be modified by the partial substitution of other metal oxides into BaTiO_3 so as to yield solid solutions. For example, dopant substitutions can change cell dimensions and hence the temperatures at which these phase changes occur. Doped BaTiO_3 has found wide applications⁸ in PTC (positive temperature coefficient) thermistors, semiconductors, and piezoelectric devices.

Different physical properties of perovskite-phase materials are related to their phase transitions, which in turn are sensitive to variables such as chemical composition, purity, number of surface and bulk defects, grain size, and sintering conditions. Hence, the need to control these parameters is critical for effective quality control of the devices produced from these materials. For instance, studies have been conducted on the effect of the crystallite size on the crystalline structure

adopted by BaTiO_3 . As an example, crystals of BaTiO_3 are often cubic at their surface but tetragonal in the bulk, with the two phases separated by a transition zone. As the crystallite size decreases below a few micrometers, the proportion of the crystal influenced by the surface effect increases and any undistorted tetragonal phase disappears. Thus, if the crystallite is small enough (nanosized), then the ferroelectric state disappears altogether and is replaced by a pseudocubic, super-paraelectric state.⁹

Perovskite-type oxides with typically very high melting points also exhibit a number of interesting chemical properties including heterogeneous catalytic activity. For example, these oxides are often utilized for CO oxidation, oxidation of hydrocarbons and chlorinated volatile organic compounds, partial oxidation of methane to synthesis gas, N_2O decomposition, NO_x reduction, hydrogenation reactions of alkenes, SO_2 reduction, as well as in various types of electro- and photocatalytic reactions.^{10,11}

There is a variety of dense perovskite-phase mixed-metal oxides, which are capable of high oxygen transport fluxes at elevated temperatures ($T > 600$ °C). At high temperatures, the oxygen permeability of some of these materials can exceed that of porous membranes. For instance, LiNbO_3 (**Aldrich Prod. No. 254290**), SrCeO_3 , and SrTiO_3 (**Aldrich Prod. No. 517011**) are examples of perovskite-type oxides that have been successfully used for oxygen transport. Membranes created from these materials are dense and as a result, their separation selectivity for oxygen is highly promising. In particular, the oxygen-transport mechanism for these materials involves oxidation and reduction of O_2 at the membrane surface, with diffusion of oxide ions and electrons through the dense ceramic matrix, driven by an oxygen potential difference across the membrane. The stability and high oxygen flux potential at high temperatures of these materials, not surprisingly, have provided for their consideration in a number of high-temperature membrane reactor applications, including in oxidation reactions.^{12,13}

As mentioned, ferroelectric perovskite oxides, including BaTiO_3 and SrTiO_3 , exhibit large non-linear optical coefficients, large dielectric constants, and low loss characteristics. Their novel physical properties often result from strong electron-electron interactions. Because these effects are dependent on structure and finite size (e.g., the ferroelectric transition temperature of isolated grains may decrease for average grain parameters of about 200 nm),^{14,15} considerable effort has been expended in the rational synthesis (in terms of size, shape, and morphology) of pure crystals and of thin films of these ferroelectric oxides.¹⁶⁻¹⁸ As compared with bulk ferroelectrics, low-dimensional nanoscale ferroelectric structures may increase the storage density of nonvolatile ferroelectric random access memories (NVFRAMs) by as much as a factor of 5.¹⁹



Applications of Perovskite-phase Metal Oxide Materials

The properties and applications²⁰ of a number of important perovskite-phase mixed-metal oxides are summarized in **Table 1**. The uses for these materials are based upon their intrinsic dielectric, ferroelectric, piezoelectric, and pyroelectric properties of relevance in corresponding electronics applications such as electromechanical devices, transducers, capacitors, actuators, high-k dielectrics, dynamic random access memory, field effect transistors, and logic circuitry.^{1,21,22} All ferroelectric materials are both pyroelectric and piezoelectric with the potential for additional utility based upon these properties.

Table 1. Perovskite-phase Metal Oxides: Properties and Applications

| Materials | Properties | Applications |
|--|--|--|
| BaTiO ₃ | dielectric | capacitor, sensor |
| (Ba,Sr)TiO ₃ | pyroelectric | pyrodetector |
| PbTiO ₃ | pyroelectric piezoelectric | pyrodetector, acoustic transducer |
| Pb(Zr,Ti)O ₃ | dielectric pyroelectric piezoelectric electro-optic | nonvolatile memory, pyrodetector surface acoustic wave device, substrate waveguide device |
| (Pb,Li)(Zr,Ti)O ₃ | pyroelectric electro-optic | pyrodetector waveguide device, optical memory display |
| LiNbO ₃ | piezoelectric | pyrodetector, surface acoustic wave device |
| (LiNbO ₃ /Ti) | electro-optic | waveguide device, second harmonic generation, optical modulator |
| K(Ta,Nb)O ₃ | pyroelectric electro-optic | pyrodetector waveguide device, frequency doubler |
| Pb(Mg _{1/3} Nb _{2/3})O ₃ | dielectric | memory, capacitor |

For instance, ferroelectric materials can have their polarization reversed (switched) for memory applications at or near T_C . In particular, the drive for size reduction in electronic components has led to the development of ceramic capacitors, especially the multilayer ceramic capacitor (MLCC), using ceramic dielectric materials with the highest permittivity values. More complicated multilayer configurations have also been devised to fulfill the growing technological need for increased capacitance within an ever smaller confinement space.²³ In recent years, MLCCs possessing a capacitance of 1 to 100 μF have been produced with internal Ni electrodes, which are composed of 500 or more laminated thin dielectric layers of $\sim 2 \mu\text{m}$.⁸

Another area attracting a good deal of interest has been the use of ferroelectric thin films as nonvolatile computer memories.²⁰ Current static and dynamic memory chips lose data they contain when the power to the memory component is interrupted, often resulting in an irretrievable loss of information. Magnetic storage facilities provide one answer to this problem, but the need for fast, lightweight memories with low power consumption integrated into silicon chips is important for some applications. These materials would also in theory be unaffected by radiative and magnetic fields, which can destroy the data stored on a standard memory chip. There are two key designs for a nonvolatile memory which utilize ferroelectric materials, namely lateral configuration and vertical configuration. One of the main features of these architectures is the nondestructive readout method, which has been a general problem for these types of memory devices. In other words, to read the memory cell, it must be poled, which can invariably erase the information the cell contained. This drawback can be overcome by designing a system, so as to subsequently rewrite the information back into the memory once the cell has been initially read.

Another application currently under investigation is the use of ferroelectric materials as electro-optic switching devices for optical computers.^{13,20} This idea is based upon the ability of a ferroelectric material to change its refractive index under an applied field. The response of this material for electro-optic applications is influenced by many factors such as film thickness, wavelength of the light, and the properties of the electrodes. Another application for thin films would be

as read/write optical storage devices. In this case, the material, such as lead lanthanum zirconate titanate (PLZT), is switched between its ferroelectric state and its antiferroelectric state upon the application of a light beam, while the film is simultaneously under the influence of an applied field. The signal-to-noise ratio, which is typically poor for thin films, can be significantly increased in these particular thin PLZT film systems ($\sim 0.5 \mu\text{m}$) under conditions that optimize interference effects. This type of optical storage device is relatively unaffected by the presence of magnetic fields and thus, can be considered as the optical equivalent of magnetic hard disks in computers.

Controlling the Physical Properties of Perovskite-phase Materials

The physical properties of these materials are often tailored through formation of either nonintegral stoichiometric phases or solid solutions. Because metallic conductivity in perovskites is due to the strong cation-anion-cation interaction, altering the structure of these materials through chemical substitution can have a dramatic effect on local order and the properties of the resulting material. The CaTiO₃-SrTiO₃ system is a model example.^{24,25} Strontium titanate is a cubic perovskite whereas calcium titanate (**Aldrich Prod. No. 633801**) is an orthorhombically distorted perovskite. In the combined Ca_xSr_{1-x}TiO₃, where Ca⁺² is substituted at the Sr⁺² site, the value of 'x' has a dramatic effect not only on the dielectric constant but also on the phases of the material, which may range from orthorhombic to tetragonal to cubic.²⁶⁻²⁸ Whether this material undergoes ferroelectric or antiferroelectric phase transitions depends on its exact chemical composition.²⁹ As an example of the significance of this synthetic capability, the availability of nanosized Ca_{0.7}Sr_{0.3}TiO₃ particles may enhance the material's existing usage as an efficient dielectric barrier for the plasma-induced, catalyst-free decomposition of CO₂.²⁸

Molten Salt Synthesis of Perovskite-phase Materials

While bulk materials have long been prepared using the molten salt synthesis (MSS) method, the preparation of uniform nanostructures using this technique has only arisen within the current century. Antonietti et al.³⁰ first described a 'convenient route for the synthesis of nanoparticulate salts, metals and metal oxides' using concentrated salt solutions and block copolymer surfactants. Research groups in Asia³¹⁻³³ subsequently demonstrated the high-yield preparation of smooth single-crystalline Mn₃O₄ (**Aldrich Prod. No. 377473**), SnO₂ (**Aldrich Prod. No. 549657**), and CuO (**Aldrich Prod. No. 544868**) one-dimensional nanostructures through the MSS method using NaCl in the presence of a surfactant (such as TWEEN® 80 and Triton® X-100), and found that an Ostwald ripening mechanism (namely the selective dissolution of fine particles and redeposition onto larger particles) was primarily responsible for the nanowire growth observed.

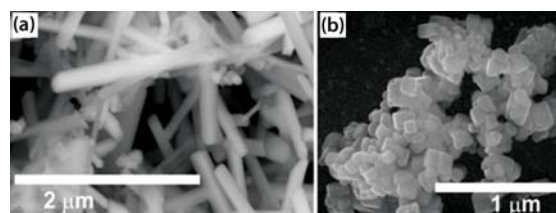
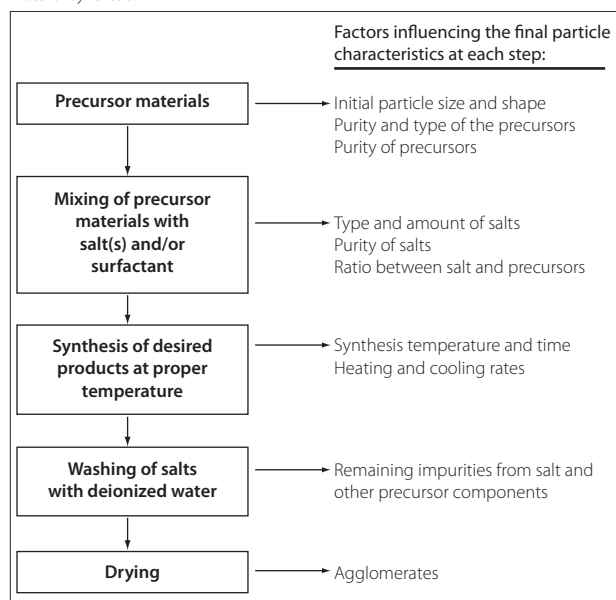


Figure 1. SEM images of BaTiO₃ nanorods and SrTiO₃ nanocubes.

In our laboratory, the MSS reaction has been used to prepare pristine BaTiO₃ nanostructures (including nanowires) with diameters ranging from 50 to 80 nm and with aspect ratios ranging from 1:1 to larger than 25:1, as well as single-crystalline SrTiO₃ nanocubes with a mean edge

length of 80 nm (Figure 1). The MSS method is one of the simplest, most versatile, and cost-effective approaches available for obtaining crystalline, chemically-purified, single-phase powders in high yield, often at lower temperatures and in overall shorter reaction times with little residual impurities as compared with conventional solid-state reactions.³⁴ The appeal of this technique arises from its intrinsic scalability, generalizability, and facility as well as its fundamental use of salt as the reaction medium.³⁴ In fact, as summarized in Table 2, (i) the identity as well as the size of the anion associated with the salt, (ii) the solubilities/dissolution rates of the constituent components within the molten salt itself, (iii) the precise melting point of either the salt or complex salt mixture used, (iv) heating temperature and duration, as well as (v) the unique morphological (e.g., shape) and chemical composition of the precursors involved are all important, readily controllable factors that can influence the growth rate as well as the resultant structural characteristics (i.e., size, shape, and crystallinity) of the as-prepared particles.³⁴⁻³⁶

Table 2. Flow chart and factors influencing the MSS method for perovskite-phase material synthesis.



MSS is a simple, readily scaleable (in terms of grams) solid-state reaction in the presence of NaCl and a non-ionic surfactant, i.e., NP-9 (nonylphenyl ether). The following reactions (Equation 1 and Equation 2) summarize a postulated mechanism for the synthesis of these nanomaterials. Here, the term 'M' (the metal species) can represent either Ba or Sr, as relevant examples.



The importance of the experimental conditions used to form these nanostructures cannot be underestimated. It is noteworthy that for BaTiO₃ and SrTiO₃ in particular, the use of different precursors, such as oxides and chlorides, as opposed to oxalates, produces neither phase-pure titanates nor even nanostructures. Even a slight change of conditions, such as running the reaction at a lower temperature, i.e., 810 °C (below the melting point of NaCl), results in a lack of phase-pure titanates. The thermal effect can be rationalized by the change in the viscosity in the growth medium, which decreases when the temperature increases.

Additional experimental results³⁷ demonstrate that, while maintaining identical experimental conditions (i.e., same ionic strength, temperature, and/or surfactant) but altering the metal precursor used, different shapes of perovskite nanostructures can be synthesized. These data are suggestive of the importance of interfacial energies between the constituents and the salt medium itself in determining the ultimate product morphology obtained. In fact, the shape of a nanocrystal is determined by the relative specific surface energies associated with the facets of the crystal. That is, with barium, nanowires can be fabricated whereas with strontium, nanocubes are normally synthesized. The ultimate shape of a single crystalline nanostructure reflects the intrinsic symmetry of the corresponding lattice.

The MSS method has also been used to prepare a series of single-crystalline Ca_{1-x}Sr_xTiO₃ (0 ≤ x ≤ 1) nanoparticles.^{38,39} Shapes of the generated Ca_{1-x}Sr_xTiO₃ nanoparticles alter from cubes to quasi-spheres with decreasing x values. Typical nanoparticles (Figure 2) have sizes ranging between 70 and 110 nm, irrespective of the Sr or Ca content. The precise chemistry of the resulting nanoparticles is readily tunable by adjusting the ratio of the reactants. This capability to generate materials of a desired doping level should enable future investigations of the composition-dependent properties of these materials. For instance, nanocubes of SrTiO₃, measuring 80 ± 10 nm, show strong first-order Raman scattering, unlike the bulk. Moreover, rapid polarization fluctuations within the nanoscopic ferroelectric regions in these materials can interfere with a polar phonon, resulting in a Fano-like asymmetric line shape in these SrTiO₃ nanocubes as well as in Ca_{0.3}Sr_{0.7}TiO₃.³⁹

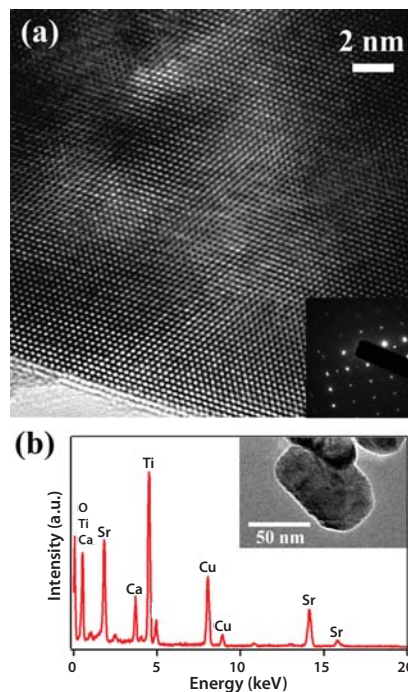


Figure 2. (a) HRTEM image of a Ca_{0.3}Sr_{0.7}TiO₃ nanoparticle. Inset of (a) is a SAED pattern of a Ca_{0.3}Sr_{0.7}TiO₃ nanoparticle. (b) EDS data of the as-synthesized Ca_{0.3}Sr_{0.7}TiO₃ nanoparticle. Inset of (b) is a typical TEM image of the as-prepared Ca_{0.3}Sr_{0.7}TiO₃ nanoparticle sample.



Rational control over the actual shape of perovskite metal oxides has recently been achieved for single-crystalline BaZrO₃ (Aldrich Prod. No. 631884) particles⁴⁰ through the MSS methodology using a NaOH/KOH salt mixture (Figure 3). The evolution of particle morphology from predominantly cubes to a mixture of cubes and spheres and finally to solely spheres has been demonstrated by increasing annealing/reaction times at suitable annealing temperatures, all other parameters being equal. Manipulating the shape of perovskite oxides is of great importance due to their strongly structure-dependent physical properties.^{41,42} For instance, as-prepared, submicron-scale samples possessed a noticeably higher photoluminescence (PL) efficiency as compared with bulk, and in particular, spheres evinced a better PL signal as compared with cubes.

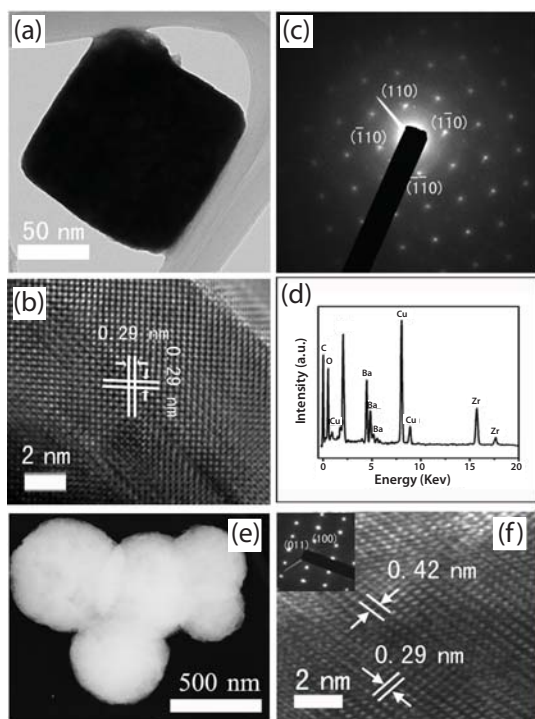


Figure 3. BaZrO₃ cubes: (a) Typical TEM image; (b) HRTEM image of a portion of the cube in (a) with zone axis corresponding to [001]; (c) SAED pattern of cube sample; (d) EDS. The Cu and C peaks originate from the TEM grid. BaZrO₃ spheres: (e) Typical TEM micrograph; (f) HRTEM image of a portion of one of the spheres in (e) corresponding to the zone axis of [011]. Inset of (f) is the associated SAED pattern.

In additional experiments,⁴³ we noted that the production of relatively high quality barium zirconate samples was generally favored by high annealing temperatures, slow cooling rates, and overall long reaction times. In terms of optimal overall reaction conditions, the most uniform, crystalline, well-dispersed, and chemically homogeneous BaZrO₃ sub-micron-sized particles were obtained using BaC₂O₄ (Aldrich Prod. No. 456004) and ZrO₂ as precursors; NaOH/KOH as the molten reaction medium; a molar ratio of BaC₂O₄:ZrO₂:salt corresponding to 1:1:20; a heating rate of 5 °C/min; as well as a reaction temperature of 720 °C. Shorter annealing times (e.g., 30 min) coupled with higher cooling rates (e.g., 100 °C/min) led to the production of smaller-sized cubic

particles. By contrast, longer annealing times (e.g., 60-210 min) and/or slower cooling rates (e.g., 5 °C/min) induced particle conversion from cubes to spheres and usually resulted in a mixture of cubic and spherical morphological motifs. Moreover, either increasing the annealing time or slowing the cooling rates resulted in the formation of larger-sized spherical particles.

Future work in this area will involve the detailed investigation of ferroelectricity, piezoelectricity, and paraelectricity at the nanoscale, as well as mechanistic studies of the formation and growth of these nanostructures for the purposes of synthetic optimization. More specifically, these efforts will concentrate on understanding structure-property correlations in perovskite nanostructures.

References

- Hill, N. A. *J. Phys. Chem. B* **2000**, *104*, 6694.
- Scott, J. F. *Ferroelectr. Rev.* **1998**, *1*, 1.
- Millis, A. J. *Nature* **1998**, *392*, 147.
- Chandler, C. D.; Roger, C.; Hampden-Smith, M. J. *Chem. Rev.* **1993**, *93*, 1205.
- Smart, L.; Moore, E. *Solid State Chemistry: an Introduction*, 2nd ed.; Chapman & Hall: London; New York, 1995.
- West, A. R. *Basic Solid State Chemistry*, 2nd ed.; John Wiley & Sons: New York, 1999.
- Song, T. K.; Kim, J.; Kwun, S.-I. *Solid State Commun.* **1996**, *97*, 143.
- Vojatovic, M. M.; Bobic, J., D.; Stojanovic, B. D. *Science of Sintering* **2008**, *40*, 235.
- Arlt, G.; Hennings, D.; de With, G. *J. Appl. Phys.* **1985**, *58*, 1619.
- Kiennemann, A.; Petit, C.; Roger, A. C.; Pitchon, V. *Curr. Topics in Catal.* **2002**, *3*, 147.
- Lombardo, E. A.; Ulla, M. A. *Res. Chem. Intermed.* **1998**, *24*, 581.
- Perez-Ramirez, J.; Vigeland, B. *Angew. Chem. Int. Ed.* **2005**, *44*, 1112.
- Chung, S.-Y.; Kim, I.-D.; Kang, S.-J. *Nat. Mater.* **2004**, *3*, 774.
- Hornebecq, V.; Huber, C.; Maglione, M.; Antonietti, M.; Elissalde, C. *Adv. Funct. Mater.* **2004**, *14*, 899.
- Fu, H.; Bellaiche, L. *Phys. Rev. Lett.* **2003**, *91*, 257601.
- Willis, L. A.; Wessels, W.; Richeson, D. S.; Marks, T. J. *Appl. Phys. Lett.* **1992**, *60*, 41.
- Zhang, J.; Beetz, C. P. J.; Krupanidhi, S. B. *Appl. Phys. Lett.* **1994**, *65*, 2410.
- Zhao, J.; Fuffygin, V.; Wang, F.; Norris, P. E.; Bouthiette, L.; Woods, C. J. *Mater. Chem.* **1997**, *7*, 933.
- Naumov, I. I.; Bellaiche, L.; Fu, H. *Nature* **2004**, *432*, 737.
- Auciello, O.; Scott, J. F.; Ramesh, R. *Phys. Today* **1998**, *51*, 22.
- Schrott, A. G.; Misewich, J. A.; Nagarajan, V.; Ramesh, R. *Appl. Phys. Lett.* **2003**, *82*, 4770.
- Tao, S.; Irvine, J. T. S. *Nat. Mater.* **2003**, *2*, 320.
- Hennings, D.; Klee, M.; Waser, R. *Adv. Mater.* **1991**, *3*, 334.
- Ranjan, R.; Pandey, D. *J. Phys.: Condens. Matter.* **1999**, *11*, 2247.
- Qin, S.; Becerro, A. I.; Seifert, F.; Gottsmann, J.; Jiang, J. *J. Mater. Chem.* **2000**, *10*, 1609.
- Ball, C. J.; Begg, B. D.; Cookson, D. J.; Thorogood, G. J.; Vance, E. R. *J. Solid State Chem.* **1998**, *139*, 238.
- Ranjan, R.; Pandey, D.; Schuddinck, W.; Richard, O.; De Meulenaere, P.; Van Landuyt, J.; Van Tendeloo, G. *J. Solid State Chem.* **2001**, *162*, 20.
- Li, R.; Tang, Q.; Yin, S.; Yamaguchi, Y.; Sato, T. *Chem. Lett.* **2004**, *33*, 412.
- Ranjan, R.; Pandey, D.; Lalla, N. P. *Phys. Rev. Lett.* **2000**, *84*, 3726.
- Wilbert, M.; Rothe, R.; Landfester, K.; Antonietti, M. *Chem. Mater.* **2001**, *13*, 4681.
- Wang, Y.; Lee, J. Y. *J. Phys. Chem. B* **2004**, *108*, 17832.
- Wang, W.; Xu, C.; Wang, G.; Liu, Y.; Zheng, C. *Adv. Mater.* **2002**, *14*, 837.
- Liu, Y.; Zheng, C.; Wang, W.; Yin, C.; Wang, G. *Adv. Mater.* **2001**, *13*, 1883.
- Hayashi, Y.; Kimura, T.; Yamaguchi, T. *J. Mater. Sci.* **1986**, *21*, 757.
- Yoon, K. H.; Cho, Y. S.; Kang, D. H. *J. Mater. Sci.* **1998**, *33*, 2977.
- Zboril, R.; Mashlan, M.; Petridis, D. *Chem. Mater.* **2002**, *14*, 969.
- Mao, Y.; Banerjee, S.; Wong, S. S. *J. Am. Chem. Soc.* **2003**, *125*, 15718.
- Mao, Y.; Wong, S. S. *Adv. Mater.* **2005**, *17*, 2194.
- Banerjee, S.; Kim, D.-I.; Robinson, R. D.; Herman, I. P.; Mao, Y.; Wong, S. S. *Appl. Phys. Lett.* **2006**, *89*, 223130.
- Zhou, H.; Mao, Y.; Wong, S. S. *J. Mater. Chem.* **2007**, *17*, 1707.
- Buhro, W. E.; Colvin, V. L. *Nature Mater.* **2003**, *2*, 138.
- Peng, X.; Manna, L.; Yang, P.; Wickham, J.; Scher, E.; Kadavanich, A.; Alivisatos, A. P. *Nature* **2000**, *404*, 59.
- Zhou, H.; Mao, Y.; Wong, S. S. *Chem. Mater.* **2007**, *19*, 5238.

Titanate and Zirconate Nanopowders

For a complete list of available nanopowders, please visit aldrich.com/nanomaterials

| Name | Formula | Particle Dimension | Cat. No. |
|--------------------------|--|--------------------------------|---------------------------|
| Aluminum titanate | Al ₂ O ₃ ·TiO ₂ | <25 nm (BET) | 634131-20G 634131-100G |
| Calcium titanate | CaTiO ₃ | <100 nm (BET) <50 nm (XRD) | 633801-25G |
| Strontium titanate | SrTiO ₃ | <100 nm | 517011-50G |
| Barium titanate(IV) | BaTiO ₃ | <100 nm (BET) | 467634-25G 467634-100G |
| Lithium titanate, spinel | Li ₄ Ti ₅ O ₁₂ | <100 nm (TEM) <100 nm (BET) | 702277-25G |
| Calcium zirconate | CaZrO ₃ | <50 nm (BET) <25 nm (XRD) | 631965-25G |
| Barium zirconate | BaZrO ₃ | <50 nm | 631884-25G |
| Zinc titanate | ZnTiO ₄ · ZnTiO ₂ | <50 nm (XRD) <100 nm (BET) | 634409-25G 634409-100G |

Other Titanate, Zirconate and Niobate Powders

For a complete list of available titanate, zirconate, and niobate powders, please visit aldrich.com/ceramics

Titanates

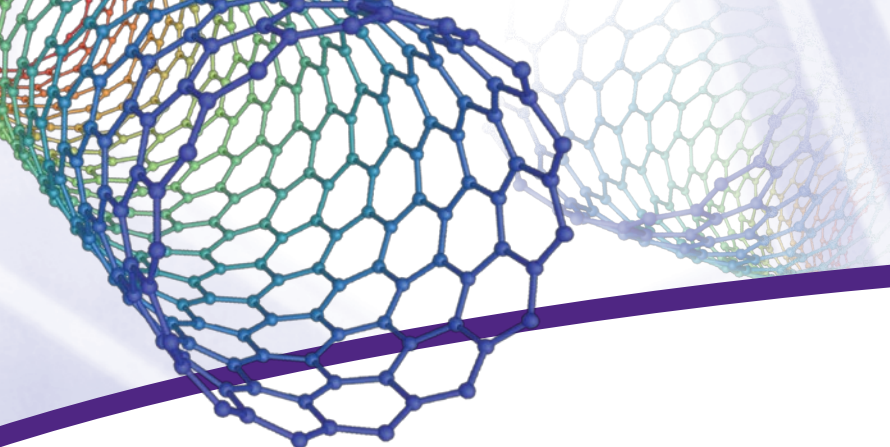
| Name | Formula | Description | Cat. No. |
|-------------------------|---|--|----------------------------|
| Barium titanate(IV) | BaTiO ₃ | ≥98.0%, particle size <3 μm | 11848-1KG |
| Neodymium(III) titanate | 2Nd ₂ O ₃ · 5TiO ₂ | particle size –325 mesh | 403695-500G |
| Iron(II) titanate | FeTiO ₃ | 99.9%, particle size –100 mesh | 400874-25G |
| Lithium titanate | Li ₂ TiO ₃ | particle size –325 mesh | 400939-100G 400939-500G |
| Lead(II) titanate | PbTiO ₃ | ≥99%, particle size <5 μm | 215805-250G |
| Bismuth(III) titanate | Bi ₂ O ₃ ·2TiO ₂ | particle size –325 mesh | 403687-100G |
| Barium titanate(IV) | BaTiO ₃ | 99.995% trace metals basis | 256552-10G |
| Strontium titanate | SrTiO ₃ | 99%, particle size 5 μm | 396141-100G 396141-500G |
| Barium titanate(IV) | BaTiO ₃ | 99.9% trace metals basis, particle size <2 μm | 338842-100G 338842-500G |
| Barium titanate(IV) | BaTiO ₃ | 99%, particle size <3 μm | 208108-500G 208108-2KG |

Zirconates

| Name | Formula | Purity | Cat. No. |
|--------------------|----------------------------------|--|---------------------------|
| Lead(II) zirconate | PbZrO ₃ | 99% trace metals basis, particle size –325 mesh | 398888-50G 398888-250G |
| Barium zirconate | BaZrO ₃ | particle size <10 μm | 383309-250G |
| Lithium zirconate | Li ₂ ZrO ₃ | particle size –80 mesh | 400920-25G |
| Sodium zirconate | Na ₂ ZrO ₃ | particle size –200 mesh | 400661-25G |

Niobates

| Name | Formula | Purity (mesh) | Cat. No. |
|------------------------|---|---|-------------------------|
| Zinc niobate | Zn(NbO ₃) ₂ | 97% | 548588-50G |
| Lead magnesium niobate | (PbO) ₃ (MgO)(Nb ₂ O ₅) | ≥99% | 672874-25G |
| Lithium niobate | LiNbO ₃ | 99.9% trace metals basis, particle size 200 mesh | 254290-10G |
| Potassium niobate | KNbO ₃ | - | 541206-25G |
| Sodium niobate | NaNbO ₃ | 99.9%, particle size –100 mesh | 400653-5G 400653-25G |



Pressure Filter Reactor Systems

Applications

- Oxidation/reduction reactions where the particulate can be drawn down to a filter cake
- Nanotechnology where the material must be contained and the filtrate is the actual product or nanoparticle needed
- Simple Bioreactor as gases can be introduced through pressure head via a pressure or NPT fittings and tubing
- Paints/pigments other viscous solutions

Pressure Filter Reactor Systems

Rugged heavy-wall reactors with a Schott flange with shallow o-ring groove at the top for connection to a jointed head with quick-release clamp. These complete bench top systems include all components required for operation except an IKA® stirrer motor, model RW 20.n (Prod. No. Z645087), which is recommended for all reactor sizes.

Choice of Two Models

Pressure Filter Reactor — rated 35 psig @ 100 °C, Ace Threds allow use of vacuum or pressure to drain liquid from reactor, 2 × #15 and 1 × #7 Ace Threds on 60 mm head, 3 × #15 and 1 × #7 Ace Threds on 100 mm head

Jacketed Pressure Filter Reactor — as above with jacket for heating or cooling reaction

| Type | Prod. No. | Capacity |
|----------|-----------|----------|
| Standard | Z564079 | 600 mL |
| | Z564109 | 1 L |
| | Z564133 | 2 L |
| Jacketed | Z564087 | 600 mL |
| | Z564117 | 1 L |
| | Z564141 | 2 L |



For more information, please visit sigma-aldrich.com/labware

IKA is a registered trademark of IKA Works, Inc.

Sigma-Aldrich® Worldwide Offices

Argentina

Free Tel: 0810 888 7446
Tel: (+54) 11 4556 1472
Fax: (+54) 11 4552 1698

Australia

Free Tel: 1800 800 097
Free Fax: 1800 800 096
Tel: (+61) 2 9841 0555
Fax: (+61) 2 9841 0500

Austria

Tel: (+43) 1 605 81 10
Fax: (+43) 1 605 81 20

Belgium

Free Tel: 0800 14747
Free Fax: 0800 14745
Tel: (+32) 3 899 13 01
Fax: (+32) 3 899 13 11

Brazil

Free Tel: 0800 701 7425
Tel: (+55) 11 3732 3100
Fax: (+55) 11 5522 9895

Canada

Free Tel: 1800 565 1400
Free Fax: 1800 265 3858
Tel: (+1) 905 829 9500
Fax: (+1) 905 829 9292

Chile

Tel: (+56) 2 495 7395
Fax: (+56) 2 495 7396

China

Free Tel: 800 819 3336
Tel: (+86) 21 6141 5566
Fax: (+86) 21 6141 5567

Czech Republic

Tel: (+420) 246 003 200
Fax: (+420) 246 003 291

Denmark

Tel: (+45) 43 56 59 00
Fax: (+45) 43 56 59 05

Finland

Tel: (+358) 9 350 9250
Fax: (+358) 9 350 92555

France

Free Tel: 0800 211 408
Free Fax: 0800 031 052
Tel: (+33) 474 82 28 88
Fax: (+33) 474 95 68 08

Germany

Free Tel: 0800 51 55 000
Free Fax: 0800 64 90 000
Tel: (+49) 89 6513 0
Fax: (+49) 89 6513 1160

Hungary

Ingyenes telefonszám: 06 80 355 355
Ingyenes fax szám: 06 80 344 344
Tel: (+36) 1 235 9063
Fax: (+36) 1 269 6470

India

Telephone
Bangalore: (+91) 80 6621 9400
New Delhi: (+91) 11 4358 8000
Mumbai: (+91) 22 4087 2364
Hyderabad: (+91) 40 4015 5488
Kolkata: (+91) 33 4013 8000

Fax

Bangalore: (+91) 80 6621 9550
New Delhi: (+91) 11 4358 8001
Mumbai: (+91) 22 2579 7589
Hyderabad: (+91) 40 4015 5466
Kolkata: (+91) 33 4013 8016

Ireland

Free Tel: 1800 200 888
Free Fax: 1800 600 222
Tel: (+353) 402 20370
Fax: (+353) 402 20375

Israel

Free Tel: 1 800 70 2222
Tel: (+972) 8 948 4100
Fax: (+972) 8 948 4200

Italy

Free Tel: 800 827 018
Tel: (+39) 02 3341 7310
Fax: (+39) 02 3801 0737

Japan

Tel: (+81) 3 5796 7300
Fax: (+81) 3 5796 7315

Korea

Free Tel: (+82) 80 023 7111
Free Fax: (+82) 80 023 8111
Tel: (+82) 31 329 9000
Fax: (+82) 31 329 9090

Malaysia

Tel: (+60) 3 5635 3321
Fax: (+60) 3 5635 4116

Mexico

Free Tel: 01 800 007 5300
Free Fax: 01 800 712 9920
Tel: (+52) 722 276 1600
Fax: (+52) 722 276 1601

The Netherlands

Free Tel: 0800 022 9088
Free Fax: 0800 022 9089
Tel: (+31) 78 620 5411
Fax: (+31) 78 620 5421

New Zealand

Free Tel: 0800 936 666
Free Fax: 0800 937 777
Tel: (+61) 2 9841 0555
Fax: (+61) 2 9841 0500

Norway

Tel: (+47) 23 17 60 00
Fax: (+47) 23 17 60 10

Poland

Tel: (+48) 61 829 01 00
Fax: (+48) 61 829 01 20

Portugal

Free Tel: 800 202 180
Free Fax: 800 202 178
Tel: (+351) 21 924 2555
Fax: (+351) 21 924 2610

Russia

Tel: (+7) 495 621 5828
Fax: (+7) 495 621 6037

Singapore

Tel: (+65) 6779 1200
Fax: (+65) 6779 1822

Slovakia

Tel: (+421) 255 571 562
Fax: (+421) 255 571 564

South Africa

Free Tel: 0800 1100 75
Free Fax: 0800 1100 79
Tel: (+27) 11 979 1188
Fax: (+27) 11 979 1119

Spain

Free Tel: 900 101 376
Free Fax: 900 102 028
Tel: (+34) 91 661 99 77
Fax: (+34) 91 661 96 42

Sweden

Tel: (+46) 8 742 4200
Fax: (+46) 8 742 4243

Switzerland

Free Tel: 0800 80 00 80
Free Fax: 0800 80 00 81
Tel: (+41) 81 755 2828
Fax: (+41) 81 755 2815

United Kingdom

Free Tel: 0800 717 181
Free Fax: 0800 378 785
Tel: (+44) 1747 833 000
Fax: (+44) 1747 833 313

United States

Toll-Free: 800 325 3010
Toll-Free Fax: 800 325 5052
Tel: (+1) 314 771 5765
Fax: (+1) 314 771 5757

Vietnam

Tel: (+84) 3516 2810
Fax: (+84) 6258 4238

Internet

sigma-aldrich.com



Mixed Sources
Product group from well-managed
forests, controlled sources and
recycled wood or fiber
www.fsc.org Cert no. SGS-COC-003338
© 1996 Forest Stewardship Council



*Accelerating Customers'
Success through Innovation and
Leadership in Life Science,
High Technology and Service*

Order/Customer Service (800) 325-3010 • Fax (800) 325-5052
Technical Service (800) 325-5832 • sigma-aldrich.com/techservice
Development/Custom Manufacturing Inquiries **SAFC® (800) 244-1173**
Safety-related Information sigma-aldrich.com/safetycenter

World Headquarters
3050 Spruce St.
St. Louis, MO 63103
(314) 771-5765
sigma-aldrich.com